DOKUZ EYLÜL UNIVERSITY
GRADUATE SCHOOL OF NATURAL AND APPLIED SCIENCES

MODELING AND SIMULATION OF HIGH TEMPERATURE PROTON EXCHANGE MEMBRANE FUEL CELL BASED COGENERATION SYSTEMS

by
Yağmur NALBANT

June, 2018
İZMİR

MODELING AND SIMULATION OF HIGH TEMPERATURE PROTON EXCHANGE MEMBRANE FUEL CELL BASED COGENERATION SYSTEMS

A Thesis Submitted to the
Graduate School of Natural and Applied Sciences of Dokuz Eylül University
In Partial Fulfillment of the Requirements for the Master of Science of
Department of Mechanical Engineering

by
Yağmur NALBANT

June, 2018
İZMİR

M.Sc THESIS EXAMINATION RESULT FORM

We have read the thesis entitled **"MODELING AND SIMULATION OF HIGH TEMPERATURE PROTON EXCHANGE MEMBRANE FUEL CELL BASED COGENERATION SYSTEMS"** completed by **YAĞMUR NALBANT** under supervision of **ASSOC. PROF. DR. CAN ÖZGÜR ÇOLPAN** and **ASSOC. PROF. DR. YILSER DEVRİM** and we certify that in our opinion it is fully adequate, in scope and in quality, as a thesis for the degree of Master of Science.

Assoc. Prof. Dr. Can Özgür ÇOLPAN
Supervisor

Assoc. Prof. Dr. Yılser DEVRİM
Supervisor

Asst. Prof. Dr. Levent Bilir
Jury Member

Prof. Dr. Aytunç Erek
Jury Member

Asst. Prof. Dr. M. Akif Ezan
Jury Member

Prof.Dr. Latif SALUM
Director
Graduate School of Natural and Applied Sciences

ACKNOWLEDGMENT

The author wishes to express deep gratitude to co-supervisors Assoc. Prof. Dr. Can Ozgur COLPAN and Assoc. Prof. Dr. Yilser DEVRIM for their invaluable supervision, advice, encouragement, support, and insight throughout the research process.

The author wishes to express her special thanks to her dear friends Alper Can INCE and Mustafa ERCELIK for her valuable contributions in this study.

The author thanks to The Scientific and Technological Research Council of Turkey (TUBITAK) 1001 (Grant number: 214M301) Project.

The author gratefully thanks to her parents Fatma NALBANT and Hasan NALBANT, specially her sister Damla NALBANT for their invaluable support in her entire life. Finally, the author thanks to her friend Mert ATAK for all his support.

MODELING AND SIMULATION OF HIGH TEMPERATURE PROTON EXCHANGE MEMBRANE FUEL CELL BASED COGENERATION SYSTEMS

ABSTRACT

In this thesis, a HT-PEMFC system is investigated through modeling studies at cell and system levels. Firstly, a one-dimensional, semi-empirical, and steady-state model of a HT-PEMFC fed with a gas mixture consisting of hydrogen and carbon monoxide is developed. Some parameters of this model are adjusted using empirical data, which are obtained conducting experiments on a HT-PEMFC for different values of Pt loading and cell temperature. The effects of some important parameters such as operating cell temperature, Pt loadings, percentage of PA, and the amount of CO on the performance of the fuel cell are assessed. Secondly, a mathematical model of a simple cogeneration system, which includes a HT-PEMFC stack, a heat exchanger, and a pump, is developed. After validating this model using an in-house experimental data, the effect of anode stoichiometry ratio on the electrical and simple cogeneration efficiencies are examined. In addition, the average temperature of hot water is calculated for each month in a case study. Finally, the thermodynamic model for a cogeneration system including HT-PEMFC, SMR, WGS, and burner that converts natural gas into electricity and heat is developed and investigated through energy and exergy analyses. The effects of some key parameters, e.g. steam-to-carbon ratio (SCR), fuel cell operating temperature, and anode stoichiometric ratio on the system performance namely electrical efficiency, exergetic efficiency, and cogeneration efficiency are examined parametrically using energy and exergy analyses. The exergy destructions of each component in the cogeneration system are also examined according to these parameters.

Keywords: High temperature-proton exchange membrane fuel cell, semi-empirical, modeling, PBI, PVDF, mathematical model, cogeneration, SMR, WGS, energy, exergy

YÜKSEK SICAKLIKTA ÇALIŞAN PROTON DEĞİŞİM MEMBRANLI YAKIT PİLİNE DAYALI KOJENERASYON SİSTEMLERİNİN MODELLENMESİ VE SİMÜLASYONU

ÖZ

Bu tez, bir HT-PEMFC sistemi hücre ve sistem seviyelerinde modelleme çalışmaları ile incelenmiştir. İlk olarak, hidrojen ve karbon monoksit içeren gaz karışımı ile beslenen bir HT-PEMFC'nin bir boyutlu, yarı deneysel ve kararlı durumda modeli geliştirilmiştir. Bu modelin bazı parametreleri, farklı Pt yüklemesi ve hücre sıcaklığı değerleri için bir HT-PEMFC üzerinde gerçekleşen deneysel veriler kullanılarak ayarlanmıştır. Bazı önemli parametrelerin (çalışma hücresi sıcaklığı, Pt yüklemeleri, PA yüzdesi ve CO miktarı) yakıt hücresinin performansına etkisi belirlenmiştir. İkinci olarak, bir HT-PEMFC yığını, bir ısı değiştirici ve bir pompa içeren basit kojenerasyon sistemin matematiksel modeli geliştirilmiştir. Bu model kurum içi yapılan deneysel veriler kullanılarak doğrulandıktan sonra, anot stokiyometrik oranın elektriksel ve basit kojenerasyon verimleri üzerindeki etkisi incelenmiştir. Ek olarak, bir vaka çalışmasında her ay için sıcak suyun ortalama sıcaklığı hesaplanır. Son olarak, doğal gazı elektriğe ve ısıya dönüştüren bir kojenerasyon sistemi (HT-PEMFC, SMR, WGS ve brülör içeren) için termodinamik model, enerji ve ekserji analizleri ile geliştirilmekte ve araştırılmaktadır. Bazı kilit parametrelerin (örn. buhar-karbon oranı (SCR), yakıt hücresi çalışma sıcaklığı, anot stokiyometrik oranı ve katot stokiyometrik oranı) sistem performansı üzerindeki (elektriksel verimi, ekserji verimi ve kojenerasyon verimi) etkileri enerji ve ekserji analizleri kullanılarak parametrik olarak incelenmiştir. Kojenerasyon sistemindeki her bir bileşenin ekserji yıkımları da bu parametrelere göre incelenir.

Anahtar kelimeler: Yüksek sıcaklıklı proton değişim membranlı yakıt hücresi, yarı deneysel, modelleme, PBI, PVDF, matematiksel model, kojenerasyon, SMR, WGS, enerji, ekserji

CONTENTS

Page

LIST OF FIGURES

Page

LIST OF TABLES

Page

CHAPTER ONE
INTRODUCTION

1.1 Introduction

The energy requirements in the earth are increasing more and more. In today's World, most of the energy demand is supplied using fossil fuels such as coal, natural gas, and gasoline. However, the fossil fuels have several hazards such as air pollution, climate change, and acid rains. In addition to these environmental problems, the reserves of these fuels are fast depleting. Due to these concerns, the interest in the alternative energy technologies and renewable energy resources have increased (Besancon et al., 2009; Perera, 2017).

Fuel cell, which is one of the alternative energy technologies, is an electrochemical device that directly converts chemical energy of the fuel into electrical energy. Fuel cells have several advantages over conventional power technologies (e.g. internal combustion engines and gas turbines) such as reduced dependence on fossil fuels, high electrical efficiency, and low environmental impact. Fuel cell technology has started to be used in many applications such as transportation, stationary, backup, and portable. Fuel cells can be categorized according to the type of electrolyte used, the type of fuel, the type of feeding of fuel (indirect or direct), and the operating temperature (high temperature or low temperature). The most promising technologies currently towards commercialization are Proton Exchange Membrane Fuel Cell (PEMFC) and Solid Oxide Fuel Cell (SOFC) (Barbir, 2005; Nalbant et al., 2017). When PEMFC is compared with other fuel cells, they have essential advantages such as high power density, no risk for leakage of electrolyte, low operating temperatures, easy scale-up, and short start-up time. Therefore, it can be foreseen that PEMFCs will have a significant role in the power generation in the near future (Wang et al., 2011; Wu, 2016). PEMFCs can be classified according to their operating temperature. Low-temperature PEMFCs (LT-PEMFCs) operate between 60°C and 80°C; whereas high-temperature PEMFCs (HT-PEMFCs) operate between 120°C and 200°C. HT-PEMFCs have several advantages compared to LT-PEMFCs. They have better water

and heat managements, higher carbon monoxide (CO) tolerance, and higher heat quality for cogeneration systems.

In the last two decades, the research and development activities on the HT-PEMFCs have increased; and several papers have been published on the modeling of HT-PEMFCs and HT-PEMFC based cogeneration systems. In this thesis, a semi-empirical and one-dimensional modeling of HT-PEMFC having different binders (polybenzimidazole (PBI) and polyvinylidene difluoride (PVDF)) is first developed and optimized using Excel. Then, this HT-PEMFC model is integrated into the system level model of a cogeneration system consisting of a steam-methane reformer (SMR), a water-gas shift reactor (WGS), a catalytic burner, and auxiliary components (e.g. pump, compressor, condenser, and heat exchangers).

1.2 Motivation

This thesis focuses on the modeling and simulation of HT-PEMFC at cell and system levels. The main motivations of this thesis are as follows;

- Semi-empirical modeling approach has been shown to be a powerful tool in fuel cell modeling. Although there are some mathematical models of HT-PEMFC (from 0-D to 3-D) in the literature, no study has been conducted on the semi-empirical modeling of HT-PEMFCs that compares different binders (PBI and PVDF).
- It has been shown that exergy analysis gives better insights than energy analysis for assessing the performance of energy systems. Thus, the number of studies on the exergy analysis of integrated energy system have increased significantly. However, there are no studies in the literature on the energy and exergy analyses of a HT-PEMFC based cogeneration system (including HT-PEMFC, SMR, WGS, and burner).

1.3 Objective

The main aim of this thesis is to develop a semi-empirical and one-dimensional model of HT-PEMFC having different binder types, operating cell temperatures, and Pt loadings and to integrate this model into a system-level model of a HT-PEMFC based cogeneration system. Using this system level model, energetic and exergetic assessments of a cogeneration system (including HT-PEMFC, SMR, WGS, and burner) that converts natural gas into electricity and heat for residential applications (e.g. hot water and electricity) is performed. The objectives of the thesis are listed below:

- To develop a HT-PEMFC model at the cell level to examine the effects of some important manufacturing and operating parameters (e.g. cell temperature, Pt loading, PA percentage, the amount of CO, and binder) on the cell performance.
- To develop a mathematical model for a simple cogeneration system including a HT-PEMFC stack, a heat exchanger, and a pump, and examine the effects of the anode stoichiometric ratio on the simple cogeneration system performance.
- To develop a thermodynamic model for an integrated cogeneration system (including HT-PEMFC, SMR, WGS, and burner) that converts natural gas into electricity and heat.
- To investigate the effects of some key parameters, e.g. steam-to-carbon ratio (SCR), fuel cell operating temperature, and anode stoichiometric ratio, on the performance of the integrated cogeneration system (electrical efficiency, exergetic efficiency, and cogeneration efficiency) using energy and exergy analyses.

1.4 Thesis Outline

The second chapter is devoted to the introduction of fuel cell technologies, especially Proton Exchange Membrane Fuel Cell. Chapter 2 introduces the fuel cell components (membrane, catalyst layer, and backing layers) and gives the literature review. In this review, studies on the mathematical modeling of phosphoric acid doped PBI membrane-based HT-PEMFCs, the effect of the binder on the performance of HT-

PEMFC, and the modeling of HT-PEMFC stack and HT-PEMFC stack based cogeneration system are discussed. The third chapter covers the selection of the materials used in the experiments, the preparation of the MEA, and the procedure followed in the performance tests, in detail. The fourth chapter includes mathematical modeling of the HT-PEMFCs in cell and system levels. Firstly, one-dimensional and semi-empirical modeling of HT-PEMFC is explained and modeled. Secondly, mathematical model for a HT-PEMFC stack based a simple cogeneration system is presented. Finally, thermodynamic model for the cogeneration system (including HT-PEMFC, SMR, WGS, and burner) is studied, and energy and exergy analyses are given. In the fifth chapter, the results of the semi-empirical modeling of HT-PEMFC, the mathematical model of HT-PEMFC stack based simple cogeneration system, and the thermodynamic modeling of an integrated cogeneration system are given and discussed in detail. The sixth chapter gives conclusions related to the studies in this thesis.

CHAPTER TWO
BACKGROUND AND LITERATURE REVIEW

2.1 Fuel Cells

Fuel cell is an electrochemical device that directly converts chemical energy into electrical energy. The heart of a fuel cell is the Membrane Electrode Assembly (MEA), which consists of anode, cathode, and membrane. The fuel is fed from the anode side; whereas the oxidant (air or oxygen) is fed to from the cathode side of the fuel cell. The electrochemical reactions occur in the electrochemically actives sites of anode and cathode (also known as catalyst layers). As a result of these reactions, ions and electrons are produced. The ions are transported through the membrane from one electrode to the other; whereas the electrons are transported through an external circuit. The electrons circulate through an external load continuously to produce electrical power.

The fuel cells can be classified with considering the type of fuel and electrolyte. The characteristics of these fuel cell types including their operating temperature, typical electrolyte material, charge carrier, typical catalyst material, typical interconnect material, and typical fuel is given in Table 2.1 (Colpan et al., 2018). The main types are proton exchange membrane fuel cells (PEMFCs), solid oxide fuel cells (SOFCs), direct methanol fuel cells (DMFCs), alkaline fuel cells (AFCs), and molten carbonate fuel cells (MCFCs) as shown in Figure 2.1. At the present time, most of the researches is focused on the development of PEMFCs and SOFCs.

Table 2.1 Major fuel cell types and their main components and operating conditions (Modified from Colpan et al., 2018)

	PEMFC	**SOFC**	**AFC**	**MCFC**	**DMFC**
Operating Temperature	60-200°C	600-1000°C	60-220°C	~650°C	60-80°C
Typical Electrolyte Material	Polymer Membrane	Ceramic	Liquid KOH	Molten Carbonate	Polymer Membrane
Charge Carrier	H^+	O^{2-}	OH^-	CO_3^{2-}	H^+
Typical Catalyst Material	Platinum	Nickel/yttria stabilized zirconia	Platinum	Nickel	Platinum, Platinum-Ruthenium
Typical Interconnect Material	Carbon Based	Ceramic Based	Carbon Based	Stainless Steel Based	Carbon Based
Typical Fuel	H_2	H_2, CH_4, CO	H_2	H_2, CH_4	CH_3OH

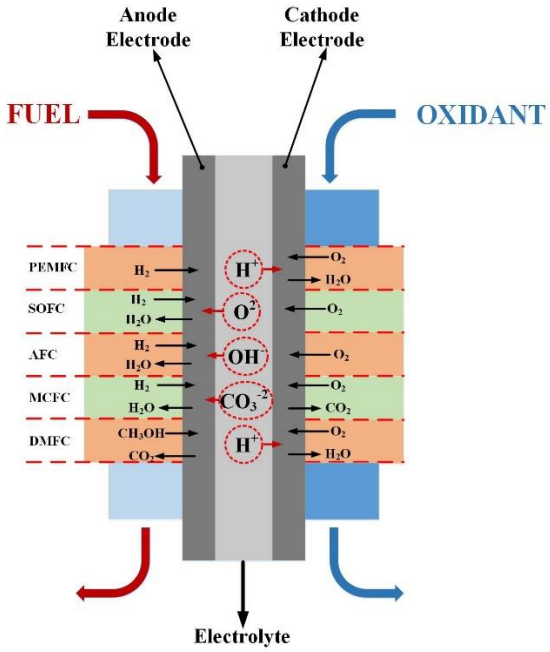

Figure 2.1 Fuel cell types (adapted from Ercelik, 2017)

2.2 Proton Exchange Membrane Fuel Cell (PEMFC)

In proton exchange membrane fuel cell (PEMFC), protons transfer through the ionic conductive membrane from the anode to the cathode. The typical catalyst used in this kind fuel cell is platinum supported on carbon (Pt/C). Eqs. (2.1) and (2.2) show

the electrochemical reactions occurring at the anode and cathode, respectively; whereas Eq. (2.3) shows the overall reaction (Colpan et al., 2018).

$$\text{Anode: } H_2 \rightarrow 2H^+ + 2e^- \quad (2.1)$$

$$\text{Cathode: } 0.5O_2 + 2H^+ + 2e^- \rightarrow H_2O \quad (2.2)$$

$$\text{Overall: } H_2 + 0.5O_2 \rightarrow H_2O \quad (2.3)$$

PEMFC can be classified into two categories according to its operating temperature. The Low Temperature-Proton Exchange Membrane Fuel Cell (LT-PEMFC) operates around 60-80°C while the High Temperature-Proton Exchange Membrane Fuel Cell (HT-PEMFC) operates between 120°C and 200°C (Rosli et al., 2017). The LT-PEMFC usually uses Nafion® produced by DuPont or another perfluorinated polymer as the membrane Water is required for activating the proton conductivity inside the Nafion® membrane. Therefore, the membrane must always be kept in a hydrated condition to maintain optimal performance (Bose et al., 2011). When the cell temperature exceeds the boiling temperature of water, water management in the fuel cell becomes more challenging. On the other hand, heat is generated in the electrochemical reaction occurring in the fuel cell. If the temperature increases too much, it will cause the membrane to dry up; and the Nafion® membrane will lose its proton conduction capability due to the increases in the proton transport resistance. Thus, water and thermal management issues play a key role in the LT-PEMFCs. In addition, CO tolerance is very low in the PEMFCs operating at low temperatures. Hence, CO poisoning phenomenon causes a significant decrease in the performance of this kind of fuel cells. In order to overcome these problems, research on HT-PEMFC technology has been advanced thanks to the developments in the novel membranes over the last decade. PA doped polybenzimidazole (PBI) membranes, which have good mechanical strength, high proton conductivity, and high thermal and chemical stabilities at high temperatures, have been conventionally used in the HT-PEMFCs without the need for humidification in reactant gases (Caglayan et al., 2016). If they are doped by a strong acid such as PA, sulphuric acid, and nitric acid, their proton conductivity increases. Among the different doping materials, PA is the most promising one because it forms a 3-D hydrogen bonding network with PBI. When the

doping level of PA in the membrane increases, the proton conductivity of membrane increases but the mechanical strength of membrane decreases (Ergun et al., 2012). As compared to LT-PEMFCs, water and thermal management is simpler and CO tolerance is more in HT-PEMFCs. Moreover, waste heat from this fuel cell can be recovered and used to produce other useful forms of energy (e.g. hot water). The major drawbacks of HT-PEMFCs are slow start-up, difficulty in thermal insulation, and higher material degradation rate (Rosli et al., 2017).

The development of PEMFC is a substantial research activity throughout world and is the most promising fuel cell technology towards commercialization. PEMFCs are used in the transportation, portable, and stationary applications. The use of PEMFC in the transportation applications (e.g. light-weight vehicles, automobiles, buses, electric powered bicycles, and material handling vehicles) has increased due to the disadvantages of internal combustion engines such as the use of fossil fuels, air pollution (due to CO_2 emissions), and climate change (due to the greenhouse gases) (Candusso et al., 2006; Krumpelt et al., 2002; Wang et al., 2011). The use of PEMFC in portable electronic devices has increased rapidly due to the long charging time and low energy power of the current battery technology. The main range of power for portable devices is 5-50 W. Since 2005, the worldwide production of portable fuel cells has developed; and the most of them are based on PEMFCs (Butler, 2009; Sohn et al., 2005; Wang et al., 2011). The use of PEMFC based systems in the stationary applications (e.g. residential/household and uninterrupted power supplies) is preferred for the purpose of continual power and heat supply. Although central power systems have high efficiency, they have many disadvantages such as inefficient waste heat utilization, costly and long-distance transport, and power losses during transmission (Arsalis et al., 2015; Najafi et al., 2015; Wee, 2007; Wang et al., 2011).

2.3 Fuel Cell Components

The most critical component of a fuel cell is MEA which consists of several layers: membrane, anode and cathode catalyst layers, and anode and cathode backing layers (gas diffusion layers) (Orogbemi et al., 2017; Al-Baghdadi, 2015; Okur et al., 2013). Components of the MEA is examined from Section 2.3.1 to Section 2.3.3 (Colpan et al., 2018).

2.3.1 Membrane

Membrane is made of a selectively permeable material that allows ions formed during the electrochemical reactions in an electrode to pass to the other electrode. The most widely used membranes in LT-PEMFCs are DuPont's Nafion® membranes which are perfluorosulfononic acid type membranes. Nafion® membranes have high proton conductivity in the hydration state. When the operating temperature of the fuel cell exceeds 90°C, the Nafion® membrane begins to dry and loses its proton conductivity property. In order to overcome this problem, novel membranes (polybenzimidazoles (PBIs) doped with strong acid) have been proposed for fuel cells working at high temperatures more than 100°C (Caglayan et al., 2016; Colpan et al., 2018; Nalbant et al., 2017).

The properties expected from a membrane can be listed as follows:

- Being highly proton conductive
- Being electrically insulated
- Eliminating or minimizing crossover of chemical species
- Chemically and mechanically stable under the operating conditions

2.3.2 Anode and Cathode Catalyst Layers

Anode catalyst layer is the layer where the oxidation reaction of the reactant (e.g. hydrogen or methanol) occurs; whereas oxygen reduction reaction (ORR) occurs at the cathode catalyst layer. Both anode and cathode catalyst layers' structures are quite

complex and optimizing these structures plays a key role in getting high performance from a fuel cell. An ideal catalyst layer should have sufficient void space for the reactants and products to reach and leave the electrochemically active area, respectively, and create paths to the adjacent layers for the effective transport of electrons and protons. The reactions in a fuel cell occur in the "triple-phase boundary", where the electrolyte, electrode, and chemical species are contact with each other. The preparation of catalyst ink and its coating plays an important role in increasing this boundary since it affects the performance of the fuel cell directly. In the literature, many catalyst ink formulations are available (Ren et al., 2000; Wilson and Gottesfeld, 1992; Zamel, 2016). These formulations involve the mixing of catalyst powder, deionized water, binder, and alcohol. Generally, carbon supported or unsupported Platinum (Pt) is used as the catalyst. In some cases, carbon supported bimetallic platinum based catalysts such as Platinum-Ruthenium (Pt-Ru) can be considered. Using Ru aids in removing the intermediates from the surface which thus hampers poisoning of precious metal (Das et al., 2015). The selection of the binder material in the catalyst layer is determined according to the material of the membrane. For example, if Nafion® is used as the membrane, Nafion® solution can be used as the binder material and added to the catalyst ink. The viscosity of the ink is also an important parameter, which should be adjusted according to the coating method.

2.3.3 Anode and Cathode Backing Layers

The layer which is located between the catalyst layer and the flow field plate is called backing layer. Carbon cloth or carbon paper is used widely as the anode and cathode backing layers (also known as gas diffusion layers). The most commonly used backing layers are manufactured by companies including AvCarb®, Toray®, SGL Group, SIGRACET®, and Freudenberg®. The main functions of the backing layers can be listed as follows (Colpan et al., 2018):

- to enable a pathway for the reactants from flow field channels to catalyst layers
- to remove the chemical species which are produced during the electrochemical reactions from the reaction areas

- to provide the mechanical support to the membrane electrode assembly (MEA)
- to supply the electrical connection between catalyst layers and flow field plates

2.4 Literature Survey

2.4.1 Mathematical Modeling of Phosphoric Acid doped PBI Membrane Based HT-PEMFCs

In recent years, several studies have focused on mathematical modeling of HT-PEMFCs to have a better understanding of the transport phenomena occurring inside the fuel cell that cannot be easily measured by experimental methods. These models provide more insights compared to experimental studies in the design and optimization of the fuel cells (Krastev et al., 2014). There are several modeling studies for phosphoric acid (PA) doped HT-PEMFCs in the literature. For example, Cheddie and Munroe (2006) developed a parametric model for a HT-PEMFC based on PBI membrane, which predicts the polarization curve for different porous media characteristics and compared the results of this model with experimental data. Scott et al. (2007) developed a one dimensional model of a HT-PEMFC that incorporates the effects of cell temperature and pressure on the diffusion coefficients, the exchange current density, the cell voltage, and the power density, and the effect of water transport on the proton conductivity of the PBI membrane. Ubong et al. (2009) investigated the effects of air stoichiometry, operation temperature, and pressure on the HT-PEMFC performance through developing a 3-D model of a fuel cell having triple serpentine flow channels. Mamlouk et al. (2011) developed a one-dimensional model of a HT-PEMFC based on PBI membranes using the principles of thermodynamics, transport phenomena and chemical kinetics and applied the thin film assumption technique. Their model exhibited very good agreement with experimental data and was used as a tool that provides in understanding the reasons behind the performance limitations for optimizing the electrode performance. Shamardina et al. (2010) developed a simple analytical model of a HT-PEMFC for investigating the crossover of reactant gases through the membrane. Chippar and Ju (2013) developed a gas crossover model for a HT-PEMFC having a PA-doped PBI membrane. In their

study, numerical simulations were conducted varying three critical parameters (temperature, current density, and gas crossover diffusivity) to investigate the effect of gas crossover on the HT-PEMFC performance. Sun et al. (2015) developed a two-dimensional and single-phase model and investigated the effects of cell temperature and the properties of mass transfer on the performance of the HTPEMFC. Moreover, the numerical model was used to analyse the effects of the cell temperature, the gas diffusion layer (GDL) porosity, and the GDL thickness on the current density. Sezgin et al. (2016) developed a three-dimensional HT-PEMFC model by using COMSOL Multiphysics for investigating the effect of some important design and operating parameters (inlet velocity of H_2 and O_2 and proton conductivity of the PBI membrane). Caglayan et al. (2016) developed a three-dimensional model of a HT-PEMFC made of PA doped PBI membrane. This model was used to investigate the effect of the cell temperature (between 100°C and 180°C) on the performance of the fuel cell. The results showed that when the temperature increases, the performance of fuel cell increases.

Among the modeling studies on HT-PEMFCs found in the literature, according to the authors' knowledge, no study has been conducted on the semi-empirical modeling of these fuel cells (Nalbant et al., 2017).

2.4.2 The Effect of the Binder on the Performance of HT-PEMFC

Catalyst layer of a HT-PEMFC consists of the catalyst (e.g. carbon supported platinum [Pt/C]), the binder (e.g. PBI, polyvinylidene difluoride [PVDF], polytetrafluoroethylene [PTFE], and Nafion®), the solvent, and the PA. The selection of the binder is a critical factor affecting the performance of the fuel cell. The binder material used in catalyst layer affects the mechanical properties, gas permeability, Pt utilization, the impregnation of PA, and oxygen oxidation reaction rate in the catalyst layer of a HT-PEMFC (Su et al., 2013a).

In the literature, several studies are found related to the effect of the binder on the performance of the HT-PEMFC. For example, Su et al. (2013a) investigated the gas

diffusion electrodes (GDEs) which were prepared with five different binders (Nafion®, PBI, PTFE, PVDF, and PBI-PVDF), to optimize the performance of PA doped PBI based HT-PEMFCs. The results of their study showed that PVDF and PTFE binders yielded higher performance compared to Nafion® and PBI binders due to their superior electrochemical properties and CL structure. In another study by Su et al. (2013b), they studied the effect of different membrane and binder types on the performance of the gas diffusion electrode (GDE), and these GDEs were analyzed using cyclic voltammetry (CV), polarization curve, durability test, and electrochemical impedance spectroscopy (EIS). The results of their study showed that the GDEs prepared with PTFE and PVDF provide better performance than those prepared with the Nafion® and PBI GDEs for all domains of the polarization curve. Ergun et al. (2012) studied the effect of two electrode preparation methods (PBI and PBI-PVDF as the binder in the catalyst ink) to determine the optimum electrode structure. Their study showed that the power output of fuel cell increases from 0.015 to 0.072 W/cm^2 when the binder is changed from PBI to PBI-PVDF. Holst-Olesen et al. (2014) studied separately the effect of PA, ATFMS, and PVDF on the specific activity (SA) of the electrochemical reaction in the cathode side (ORR) compared to PTFE. The catalysts prepared with different binder (PVDF and PTFE) and Pt loadings (28 and 38 wt%) was synthesized under the same conditions. In this study when the PVDF binder was added to commercial standard Pt/C catalyst, the SA increase of 50%. Lin et al. (2015) investigated the performance of the membrane electrode assemblies (MEAs) having different PVDF loadings in the CL for a HT-PEMFC; and found that MEA which is prepared with a suitable PVDF loading, displayed better stability and performance than the MEA having PBI binder. Galbiati et al. (2015) developed an innovative binder (PVDF) that was produced by emulsion polymerization of PVIg- PVDF nano-spheres and radiation implantation of Vinly-Imidazole (VI) groups. It was seen that using this binder increases the porosity and acid dispersion in the catalyst layer. This study showed that HT-PEMFC prepared with this PVDF binder yields better performance compared that with the conventional PVDF binder. Liang et al. (2015) studied the effect of MEA manufacturing techniques (different catalyst coating methods), binder types (PBI, PVDF, and PTFE), and Pt loading on the performance of a HT-PEMFC based on porous poly (2.5-benzimidazole) (ABPBI) membrane. The fuel cells

manufactured were tested using characterization methods such as SEM, EIS, and polarization curves. The current densities at 0.4 V was found 620 $mA \cdot cm^{-2}$, 500 $mA \cdot cm^{-2}$, and 350 $mA \cdot cm^{-2}$ for PVDF, PTFE, and PBI binders, respectively. The MEA prepare with PVDF had much better performance than the other MEAs. Brodt et al. (2016) investigated the effect of amount PVDF binder (from 20 to 80 wt%) and nanofiber in the catalyst layer on the power outputs of the beginning-of-life (BoL) and end-of-life (EoL) of a HT-PEMFC. The aim of this study is to enhance the hydrophobicity in cathode catalyst layer in order to reduce the water content at this layer and the rate of carbon corrosion through an accelerated voltage cycling experiment. It was found that if the PVDF binder content is more than 50 wt%, EoL increases, and otherwise decreases. In addition, when the amount of nanofiber in the catalyst layer increases, the power densities at all voltages increase.

Among the literature survey for different binders, no HT-PEMFC semi-empirical modeling studies have been conducted to assess the effect of PVDF binder on the fuel cell performance. In most of the studies found in the literature, the effect of different binder on the HT-PEMFC has been investigated experimentally.

2.4.3 The Modeling of HT-PEMFC Stack and HT-PEMFC Stack Based Cogeneration System

Currently, the use of fuel cells which convert chemical energy directly into electrical energy in the cogeneration systems are increasing more and more thanks to advantages of these system such as higher energy conversion efficiency, utilization of useful waste heat, and lower environmental impact. HT-PEMFC based cogeneration systems has also started getting more attention for the production of electricity and hot water in the household applications (Arsalis et al., 2011).

In recent years, several research groups have developed the modeling of HT-PEMFC based cogeneration system and have investigated the efficiency of these systems. Arsalis et al. (2011) developed the model of a micro-CHP residential system based on HT-PEMFC using the Engineering Equation Solver (EES) software. Four

parameters (fuel cell operating temperature, steam-to-carbon ratio, combustor temperature, and hydrogen stoichiometry) were studied to determine the effect of these parameters on the overall performance. The highest efficiency of the cogeneration system was found as 83.08%. Jannelli et al. (2013) compared the performance of integrated cogeneration systems based on three different PEMFCs through numerical models, which were validated using experimental data. The maximum electric and cogeneration efficiencies for HT-PEMFC based system were found as 40% and 79%, respectively; while the highest cogeneration efficiency was found as 80% for LT-PEMFC based system. This study showed that HT-PEMFC has higher electric efficiency and lower cogeneration efficiency than those of LT-PEMFC. Supra et al. (2013) designed a HT-PEMFC stack including cooling cells using heat transfer oil and experimentally investigated the temperature distribution in the HT-PEMFC. This study found that difference of the temperatures between cell and other cell is found 8.3 K. In addition, the voltage distribution exhibited similar to temperature distribution and the difference of voltages was found 0.047V. Arsalis et al. (2015) developed the model of a HT-PEMFC based micro-CHP system, which includes heat pump instead of thermal storage tank for residential demands. This system was optimized through genetic algorithm using thermophysical parameters for different loads. The efficiency of the total system was found as 81.5%. Herdem et al. (2015) modeled a HT-PEMFC based methanol reformer system for portable applications, and this model was parametrically studied to obtain the effects of some parameters (steam-to-carbon ratio, the fuel cell temperature, the current density of the fuel cell, etc.) on the performance of the fuel cell. Najafi et al. (2015) analyzed the long-term performance of a HT-PEMFC based micro-CHP system with two strategies (partialization and recovery) which used to solution the deviation of thermal and electrical generation of the system from steady state production. Ozgirgin et al. (2015) studied a model of micro-cogeneration hybrid system that consist of photovoltaic (PV) module, HT-PEMFC, electrolyzer, and batteries. This system was examined at different climatic conditions for Ankara. Zhang et al. (2016) investigated experimentally the dynamic behavior of three phases (heating, operating and cooling) for HT-PEMFC stack consist of liquid cooling. Then, the hybrid power system that consists of HT-PEMFC stack and battery, was suggested and examined for determine the time of heating and cooling that is

important in applications. Chang et al. (2017) developed the mathematical model for a CHP system that includes PEMFC, Organic Rankine Cycle (ORC), and Vapor compression cycle (VCC). The main of this study analyzed the effects of some parameters (solar radiation, cell temperature etc.) on the efficiency of system.

According to the findings of the literature survey, there are no studies on modeling of HT-PEMFC based cogeneration systems that use semi-empirical fuel cell model. In addition, the detailed exergy analysis of HT-PEMFC based cogeneration system has not found in the literature.

CHAPTER THREE
EXPERIMENTAL STUDY

3.1 Introduction

This chapter presents the selection of the materials that are used in the experiments, the preparation of the MEA, and the procedure followed in the performance tests. Experiments were carried out according to different operating cell temperature, Pt loadings, and different binder (PBI and PVDF). In order to calibrate some of the modeling parameters as discussed in Chapter Four, experiments on HT-PEMFC were carried out.

3.2 Materials

The molecular weight of PBI polymer was selected as 83,000 g/mol. N-N dimethylacetamide (CH3C(O) N(CH3)2 DMAc) and ortho-phosphoric acid (85%) were used as received. 70 wt% Pt/C catalyst (Tanaka, Japan), carbon cloth (with a microporous layer, Freudenberg, Germany), and PVDF (SigmaeAldrich) were used to prepare the MEA. The purity of gases used was 99.99% and Millipore water was used wherever required. All the chemicals were of analytical reagent grades and used as received, without further purifications (Nalbant et al., 2017).

3.3 MEA Preparation

MEAs were manufactured by ultrasonic coating technique applying the procedure given in Devrim et al. (2016). For the preparation of the MEAs, non-woven carbon cloth coated with a carbon microporous layer (Freudenberg-H2315C2) was used as the gas diffusion layer. The Pt/C is used as the anode and cathode side catalysts. A catalytic ink composed of 70% Pt on carbon black, PVDF, and DMAc as solvent was sprayed onto the carbon cloth. Before being used, these catalyst inks were ultrasonicated for at least 1 h for homogeneity. The catalyst ink was ultrasonically coated onto the PBI membrane at 80 °C by using the Sono-Tek ‘Exacta-coat’ ultrasonic spray instrument

(120 kHz). Before atomization in the nozzle (Accumist), the catalyst ink was added to a syringe pump and sprayed at a flow rate up to 0.5 ml·min^{-1}. A catalyst loading of 0.6, 1 and 1.5 mg/cm^2 were used for MEAs, both in the anode and the cathode side. PA doped PBI was used as the membrane. Generally, pure PBI membrane is a non-conductive polymer. To increase the proton conductivity, its need to be dope by strong acids such as PA. PA doping was carried out by immersing the membranes in PA at room temperature for at least 1 week. In this study, the acid doping level of the PBI membranes was determined approximately as 11 H_3PO_4 per polymer repeat unit for PBI. The mechanism of the proton conduction in H_3PO_4 doped PBI membrane network is shown in Figure 3.1. The electrodes were hot pressed onto both sides of the membrane at 150°C and 172 N/cm^2 for 5 min. The MEA preparation process steps are illustrated in Figure 3.2 (Nalbant et al., 2017).

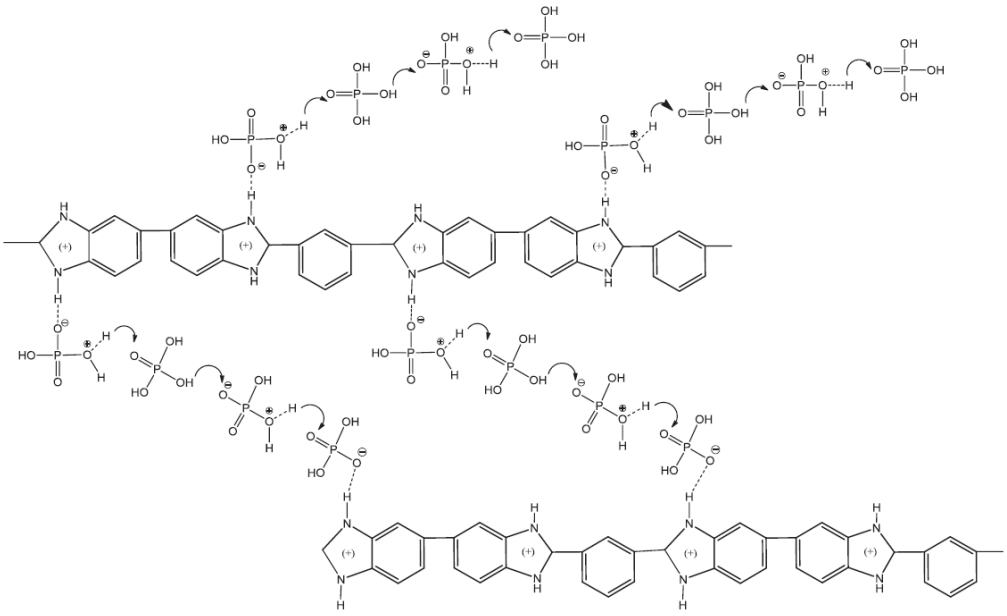

Figure 3.1 Mechanism of the proton conduction in H_3PO_4 doped PBI membrane (Devrim et al., 2018)

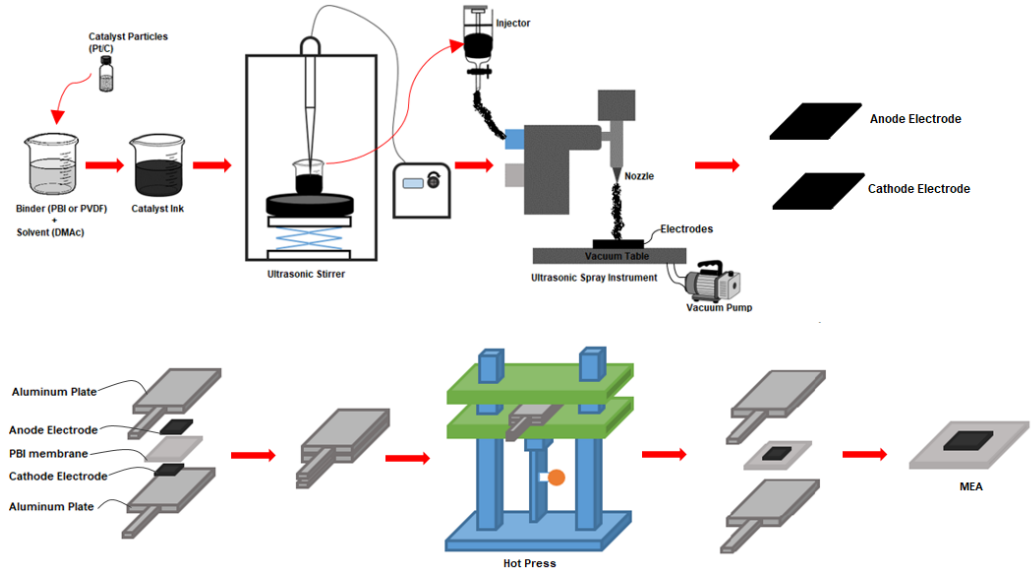

Figure 3.2 MEA preparation process steps (Nalbant et al., 2017)

3.4 HT-PEMFC Performance Tests

The performances of fabricated MEAs were measured using the HT-PEMFC (TECHYS HYGO FCTS-H2ME 500) test station, as shown in Figure 3.3. The MEAs were tested in a single HT-PEMFC hardware with a 5 cm^2 active area. The material of flow field plates was graphite. The serpentine type was used as the geometry of the flow channel on the flow field plates. During the measurements, the temperatures of the HT-PEMFC and reactant gases were set to 160°C before initiating the fuel cell test. Nonhumidified H_2/Air was fed to the system with constant stoichiometry of 1.2 for the anode side and 2.5 for the Cathode side. After steady state was achieved, the open circuit voltage (OCV) and current-voltage data were logged by changing the load. Polarization curves were obtained by measuring the current density for a given voltage by decreasing the cell voltage from OCV to 0.4 V with an interval of 0.05 V. These measurements were done after the cell reaches the steady state for each point in the polarization curve.

Figure 3.3 The HT-PEMFC (TECHYS HYGO FCTS-H2ME 500) test station (Personnel archive, 2017)

CHAPTER FOUR
MATHEMATICAL MODELING

4.1 Introduction

In recent years, several studies have focused on mathematical modeling of HT-PEMFCs to have a better understanding of the transport phenomena occurring inside the fuel cell that cannot be easily measured by experimental methods. These models provide more insights compared to experimental studies in the design and optimization of the fuel cells (Krastev et al., 2014). According to the findings of the literature survey conducted, limited 0-D to 3-D HT-PEMFC models have been developed. These models have been solved using either numerical or analytical methods. Numerical methods are generally applied to 2-D or 3-D models; whereas analytical methods are generally preferred for 0-D or 1-D models. Semi-empirical modeling approach in which experimental data are used to calibrate some modeling parameters is generally preferred for fuel cell models (e.g. 1-D models) that can be solved using analytical methods (Nalbant et al., 2017).

4.2 One-dimensional and Semi-Empirical Modeling of HT-PEMFC

One-dimensional and semi-empirical model of a HT-PEMFC fed with reformate gas was developed. The reformate gas includes H_2 and CO; whereas air includes O_2, N_2, and H_2O. The PA doped PBI was used as the membrane; and PBI or PVDF was used as the binder. When PBI or PVDF binder is used in the catalyst ink, it remains soluble in catalyst ink; therefore, the formation of agglomerates is less and the surface of CL becomes more uniform (Su et al., 2013a). Due to this reason, thin electrolyte film assumption is used for the catalyst layer (Sousa et al., 2010). The schematic diagram of a HT-PEMFC is shown in Figure 4.1. The geometric dimensions and modeling parameters in the HT-PEMFC model are tabulated in Tables 4.1 and 4.2, respectively. The main assumptions used in the model are as follows (Caglayan et al., 2016).

- The fuel cell runs at steady state and isothermal conditions.
- Ideal gas law is applied for all gases and water.
- Mass transport is only due to diffusion; and convection effects are negligible.
- None of the reactants nor products are in liquid phase.
- Membrane is impermeable to gases; thus gas crossover effect is neglected.

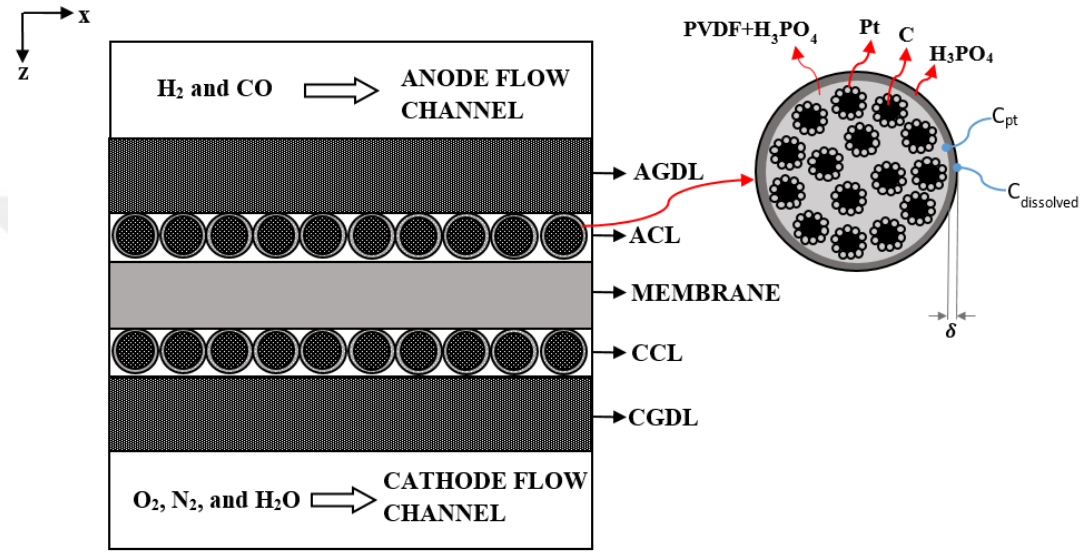

Figure 4.1 Schematic diagram of a HT-PEMFC and the catalyst layer using the thin electrolyte film assumption (Nalbant et al., 2017)

Table 4.1 The geometric dimensions in the model of the HT-PEMFC

Parameters	**Value**
Thicknesses of the anode and cathode GDL (t_{GDL})	0.55 mm
Thicknesses of the anode and cathode catalyst layers (t_{CL})	0.025 mm
Thickness of membrane (t_M)	0.075 mm
Membrane	PBI
Binder	PVDF
Thin film electrolyte	H_3PO_4
The weight percentage of PA (m^{PA})	85%

Table 4.2 The modeling parameters in the model of the HT-PEMFC at 160°C

Parameters	**Value**	**Reference**
GDL porosity (ε)	0.5	Caglayan et al., 2016
GDL tortuosity (τ)	1	-
Proton conductivity of electrolyte (σ)	0.1913 S/cm	Caglayan et al., 2016
GDL electric conductivity (σ_e)	6.875 S/cm	Caglayan et al., 2016
Operating pressures at anode and cathode (P)	1.2 atm	Caglayan et al., 2016
Anode activation energy ($E_{c,a}$)	16,900 J/mol	Authayanun et al., 2017
Cathode activation energy ($E_{c,c}$)	72,400 J/mol	Authayanun et al., 2017
Anode reference cell temperature ($T_{ref,a}$)	160°C	Sousa et al., 2010
Cathode reference cell temperature ($T_{ref,c}$)	150s°C	Sousa et al., 2010
Reference H_2 concentration on the Pt surface in the anode, $C_{Pt,a}^{ref}$	2.11 x 10^{-7} (mol/cm^3)	Sousa et al., 2010
Reference O_2 concentration on the Pt surface in the cathode, $C_{Pt,c}^{ref}$	1.07 x 10^{-7} (mol/cm^3)	Sousa et al., 2010
Anode reference exchange current density, $i_{0,a}^{ref}$	0.144 (A/cm^2)	Sousa et al., 2010
Cathode reference exchange current density, $i_{0,c}^{ref}$	2.63 x 10^{-8} (A/cm^2)	Sousa et al., 2010

4.2.1 Gas Transport in Porous Media

This model considers only one-dimensional diffusion in *z* direction. Diffusion of multicomponent gas flows through the GDL can be described using the Stefan-Maxwell equation as shown in Eq. (4.1) (Barbir, 2005). The variables at the right side of this equation is independent from *z*-direction. Thus, this equation is calculated as linear.

$$\frac{\partial X_i}{\partial z} = \frac{R \cdot T}{P} \sum_j \frac{X_i \cdot \dot{n}_j^{"} - X_j \cdot \dot{n}_i^{"}}{D_{ij}^{eff}} \tag{4.1}$$

where X_i is the mole fraction of species i, $\dot{n}_i^{"}$ is the mole flux of species i, and D_{ij}^{eff} is the effective binary diffusion coefficient for the pair i-j in the porous medium. D_{ij}^{eff} can be found using the correlation given by Slattery-Bird (1958) to account for the porosity and tortuosity effects corrected with the Bruggeman correlation (Barbir, 2005) as follows:

$$D_{ij}^{eff} = \frac{a}{P} \cdot \left(\frac{T}{\sqrt{T_{cr,i} \cdot T_{cr,j}}}\right)^{b} \cdot \left(P_{cr,i} \cdot P_{cr,j}\right)^{\frac{1}{3}} \cdot \left(T_{cr,i} \cdot T_{cr,j}\right)^{5/12} \cdot \left(\frac{1}{M_i} + \frac{1}{M_j}\right)^{1/2} \cdot \varepsilon^{\tau} \quad (4.2)$$

where T_{cr} and P_{cr} are the critical temperature and pressure of the gas, respectively. M is the molecular weight of the gas, ε is the porosity, and τ is the tortuosity. a and b are constants (a=0.0002745 and b=1.832) for diatomic gases.

4.2.1.1 Diffusion in the Porous Cathode

The chemical species in the cathode are O_2, N_2 and H_2O. The mole flux of the species can be given as follows:

$$\dot{n}_{O_2}^{"} = \frac{i}{4 \cdot F} \quad (4.3)$$

$$\dot{n}_{N_2}^{"} = 0 \quad (4.4)$$

$$\dot{n}_{H_2O,c}^{"} = 0 \quad (4.5)$$

where i is the current per geometric electrode area. Substituting the species' mole flux in Eq. (4.1), we derive

$$X_{N_2} = X_{N_2}^{0} \cdot \exp\left(\frac{R \cdot T_{cell} \cdot \dot{n}_{O_2}^{"} \cdot t_{CGDL}}{P_{cathode} \cdot D_{N_2,O_2}^{eff}}\right) \quad (4.6)$$

$$X_{H_2O,c} = X_{H_2O}^{0} \cdot \exp\left(\frac{R \cdot T_{cell} \cdot \dot{n}_{O_2}^{"} \cdot t_{CGDL}}{P_{cathode} \cdot D_{H_2O,O_2}^{eff}}\right) \quad (4.7)$$

$$X_{O_2} = 1 - \left(X_{N_2} + X_{H_2O,c}\right) \quad (4.8)$$

4.2.1.2 Diffusion in the Porous Anode

The reformate gas in the anode consists of a gas mixture of H_2, CO, CO_2, CH_4, and H_2O. The mole flux of five gases can be given as follows:

$$\dot{n}_{H_2}^{"} = \frac{i}{2 \cdot F} \quad (4.9)$$

$$\dot{n}''_{CO} = 0 \tag{4.10}$$

$$\dot{n}''_{CO_2} = 0 \tag{4.11}$$

$$\dot{n}''_{CH_4} = 0 \tag{4.12}$$

$$\dot{n}''_{H_2O} = 0 \tag{4.13}$$

Substituting mole flux of five gases in Eq. (4.1), we derive

$$X_{CO} = X^0_{CO} \cdot exp\left(\frac{R \cdot T_{cell} \cdot \dot{n}''_{H_2} \cdot t_{AGDL}}{P_{anode} \cdot D^{eff}_{CO,H_2}}\right) \tag{4.14}$$

$$X_{CO_2} = X^0_{CO_2} \cdot \exp\left(\frac{R \cdot T_{cell} \cdot \dot{n}''_{H_2} \cdot t_{AGDL}}{P_{anode} \cdot D^{eff}_{CO_2,H_2}}\right) \tag{4.15}$$

$$X_{CH_4} = X^0_{CH_4} \cdot \exp\left(\frac{R \cdot T_{cell} \cdot \dot{n}''_{H_2} \cdot t_{AGDL}}{P_{anode} \cdot D^{eff}_{CH_4,H_2}}\right) \tag{4.16}$$

$$X_{H_2O} = X^0_{H_2O} \cdot \exp\left(\frac{R \cdot T_{cell} \cdot \dot{n}''_{H_2} \cdot t_{AGDL}}{P_{anode} \cdot D^{eff}_{H_2O,H_2}}\right) \tag{4.17}$$

$$X_{H_2} = 1 - (X_{CO} + X_{CO_2} + X_{CH_4} + X_{H_2O}) \tag{4.18}$$

4.2.2 Thin electrolyte film model

The PA doped PBI membrane is used in this model. PA is used to provide paths for proton conductivity in catalyst layer and PBI membrane. PA covers catalyst agglomerates during the hot press process and forms thin electrolyte film to provide proton conductivity from CL to membrane (Liang e al., 2015). Thin electrolyte film is illustrated in Figure 4.1. The concentrations of H_2 and O_2 vary along the thin electrolyte films of anode and cathode. To obtain H_2 concentration ($C_{H_2,Pt}$) and O_2 concentration ($C_{O_2,Pt}$) at the interface between the catalyst and membrane, Fick's law of diffusion is used as follows.

$$C_{H_2,Pt} = C_{H_2,dissolved} - \left(\frac{\dot{n}''_{H_2} \cdot \delta_{anode}}{D^{PA}_{H_2} \cdot S_{Pt,anode}}\right) \tag{4.19}$$

$$C_{O_2,Pt} = C_{O_2,dissolved} - \left(\frac{\dot{n}''_{O_2} \cdot \delta_{cathode}}{D_{O_2}^{PA} \cdot S_{Pt,cathode}}\right) \quad (4.20)$$

where S_{Pt} is the surface area of Pt per geometric electrode area, D is the diffusivity and δ is the average film thickness which is obtained by calibration in this model. $C_{dissolved}$ is the equilibrium concentration derived from Henry's Law, as shown in Eqs. (4.21) and (4.22).

$$C_{H_2,dissolved} = \left(\frac{X_{H_2} \cdot P_{anode}}{H_{H_2}^{PA}}\right) \quad (4.21)$$

$$C_{O_2,dissolved} = \left(\frac{X_{O_2} \cdot P_{cathode}}{H_{O_2}^{PA}}\right) \quad (4.22)$$

where P is the pressure and H is the Henry's constant at a given temperature. The Henry's constant and diffusivity of oxygen in a concentrated PA can be given in terms of the weight percentage of PA (m^{PA}) and temperature as shown below (Chippar and Ju, 2013).

$$H_{O_2}^{PA} = 10132.5\, exp\left(257.13 \cdot (m^{PA})^2 - 431.08 \cdot (m^{PA}) + 178.45 + \frac{-93500 \cdot (m^{PA})^2 + 156646 \cdot (m^{PA}) - 64288}{T_{cell}}\right) \quad (4.23)$$

$$D_{O_2}^{PA} = 10^{-5}\, exp\left(-192.55 \cdot (m^{PA})^2 + 323.55 \cdot (m^{PA}) - 125.61 + \frac{62010 \cdot (m^{PA})^2 - 105503 \cdot (m^{PA}) + 40929}{T_{cell}}\right) \quad (4.24)$$

The Henry's constant and diffusivity of H_2 in PA are assumed to be four times and two times of those of oxygen in PA, respectively (Cheddie and Munroe, 2007).

$$H_{H_2}^{PA} = 4 \cdot H_{O_2}^{PA} \quad (4.25)$$

$$D_{H_2}^{PA} = 2 \cdot D_{O_2}^{PA} \quad (4.26)$$

4.2.3 Electrochemical model

The overall electrochemical reaction in a HT-PEMFC can be written as,

$$H_{2(g)} + \frac{1}{2} O_{2\,(g)} \rightarrow H_2O_{(g)} \tag{4.27}$$

The cell voltage (E_{cell}) can be calculated from subtracting the voltage losses, which are the activation loss at the anode ($\eta_{act,a}$), the activation loss at the cathode ($\eta_{act,c}$), and the ohmic loss (η_{ohm}) from the reversible cell voltage (E_{rev}) as shown in Eq. (4.28).

$$E_{cell} = E_{rev} - \eta_{act,a} - \left|\eta_{act,c}\right| - \eta_{ohm} \tag{4.28}$$

The reversible cell voltage is described by Nernst equation as shown in Eq. (4.29).

$$E_{rev} = E^0 + \frac{R \cdot T_{cell}}{n_{H_2} \cdot F} ln\left(\frac{(R \cdot T_{cell})^{1.5} \cdot C_{H_2,Pt} \cdot {C_{O_2,Pt}}^{0.5}}{a_{H_2O}}\right) \tag{4.29}$$

with

$$E^0 = E_0^o + \frac{(T_{cell} - T_{ref}) \cdot \Delta S^0}{n_{H_2} \cdot F} \tag{4.30}$$

where S is the entropy, T_{cell} is the cell temperature, n_{H_2} is the scaling factor of H_2, F is the Faraday constant, R is the universal gas constant, and E_0^o is the standard reference potential (at 298.15 K and 1 atm), which is equal to 1.18 V for gaseous water. $C_{H_2,Pt}$ and $C_{O_2,Pt}$ are the concentrations of H_2 and O_2 at the anode and cathode catalyst surfaces, which are calculated by the Stefan Maxwell equations and Fick's law models as shown in Section 4.2.2.

The activation losses of anode (Eq. (4.31)) and cathode (Eq. (4.32)) are calculated from Butler-Volmer equation by assuming that anode and cathode charge transfer coefficients are equal to 0.5. The effect of CO poisoning is included in the equation for anodic activation loss. The activation loss of the anode, which mainly depends on

the exchange current density of anode and the CO coverage (θ_{CO}), can be calculated as shown in Eq. (4.31) (Dhar et al., 1986).

$$\eta_{act,a} = \frac{R \cdot T_{cell}}{\alpha_a \cdot F} \, sinh^{-1}\left(\frac{i}{2 \cdot i_{0,a} \cdot (1-\theta_{CO})^2}\right) \tag{4.31}$$

$$\eta_{act,c} = \frac{R \cdot T_{cell}}{\alpha_c \cdot F} \cdot sinh^{-1}\left(\frac{i}{2 \cdot i_{0,c}}\right) \tag{4.32}$$

where α is the charge transfer coefficient and i_0 is the exchange current density, which can be calculated from Eqs. (4.33) and (4.34) for the anode and cathode, respectively. The influence of temperature on θ_{CO} in the interval of 130°C< T < 190°C can be calculated from Eq. (4.35) (Dhar et al., 1986).

$$i_{0,a} = i_{0,a}^{ref} \cdot S_{Pt,anode} \cdot \left(\frac{C_{H_2,Pt}}{C_{Pt,a}^{ref}}\right)^{\gamma_a} \cdot exp\left(\left(\frac{-E_{c,a}}{R \cdot T_{cell}}\right) \cdot \left(1 - \frac{T_{cell}}{T_{ref,a}}\right)\right) \tag{4.33}$$

$$i_{0,c} = i_{0,c}^{ref} \cdot S_{Pt,cathode} \cdot \left(\frac{C_{O_2,Pt}}{C_{Pt,c}^{ref}}\right)^{\gamma_c} \cdot exp\left(\left(\frac{-E_{c,c}}{R \cdot T_{cell}}\right) \cdot \left(1 - \frac{T_{cell}}{T_{ref,c}}\right)\right) \tag{4.34}$$

$$\theta_{CO} = 19.9 \cdot exp(-7.69 \cdot 10^{-3} \cdot T_{cell}) + 0.085 \cdot ln([CO]/[H_2]) \tag{4.35}$$

The ohmic losses are mainly caused by the resistances to the proton transfer through the membrane and the catalyst layers. The resistances to the electron transfer through the catalyst layers as well as the GDLs and the flow field plates are typically very low compared to the ionic resistances. Contact resistances, which mainly occur at the interface of GDL and flow field plates, are a function of the surface state and roughness of the material and the contact pressure between the materials. Assuming that the reduction and oxidation reactions take place at the middle of the catalyst layers (Mench, 2008), the total ohmic loss can be expressed as:

$$\eta_{ohm} = i \cdot \left(\frac{t_{ACL}/2}{\sigma \cdot \varepsilon_a} + \frac{t_M}{\sigma} + \frac{t_{CCL}/2}{\sigma \cdot \varepsilon_c}\right) + \frac{i \cdot A_{cell} \cdot R_{contact}}{A_{contact}} + i \cdot \left(\frac{t_{AGDL} + t_{CGDL} + t_{ACL}/2 + t_{CCL}/2}{\sigma_e}\right) \tag{4.36}$$

where σ is the proton conductivity of the PBI membrane, σ_e is the electric conductivity of the GDL, ε is the ionomer fraction, and t is the thickness of a layer. The relation between the proton conductivity of PA doped PBI membranes and temperature is shown in Eq. (4.37) (Bouchet and Siebert, 1999).

$$\sigma = \frac{A}{T} \cdot \exp\left(\frac{-E_a}{R \cdot T}\right) \tag{4.37}$$

where A is the pre-exponential factor, T is the temperature , and E_a is the activation energy. A and E_a are taken as $8.88\,x\,10^6$ S·K/m and -3022.6 J/mol, respectively (Caglayan et al., 2016).

Some modeling parameters in this HT-PEMFC model are calibrated using genetic algorithm with experimental data. The calibration of these parameters is shown in detailed in the Section 5.3.1.

4.3 The mathematical model for a HT-PEMFC stack based a simple cogeneration system

A mathematical model for a HT-PEMFC stack based on a simple cogeneration system is developed. This modeling study could be considered as preliminary study for an integrated cogeneration system which consists of steam-methane reformer, water-gas-shift, catalytic burner, and auxiliary components. The model developed is validated with experimental data (electrical and cogeneration efficiencies and temperature difference of coolant). The schematic diagram of the simple cogeneration system is shown in Figure 4.2, and the working parameters are tabulated in Table 4.3.

As can be seen from the Figure 4.2, this simple cogeneration system includes HT-PEMFC stack, heat exchanger, pump, and valve. HT-PEMFC stack is fed with pure H_2 at the anode side and with dry air (O_2 and N_2) at the cathode side. HT-PEMFC stack operates at 160°C and is cooled with ethylene glycol. Heated ethylene glycol is used as hot fluid in the heat exchanger and supplies heat to network water. In this section, the modeling of the main components (HT-PEMFC stack and heat exchanger (HEX))

in the cogeneration system is presented. The main assumptions used in the model are as follows:

- Each component runs at steady state conditions.
- HT-PEMFC stack is thermally insulated.
- The electrical power required for the pump has been neglected.

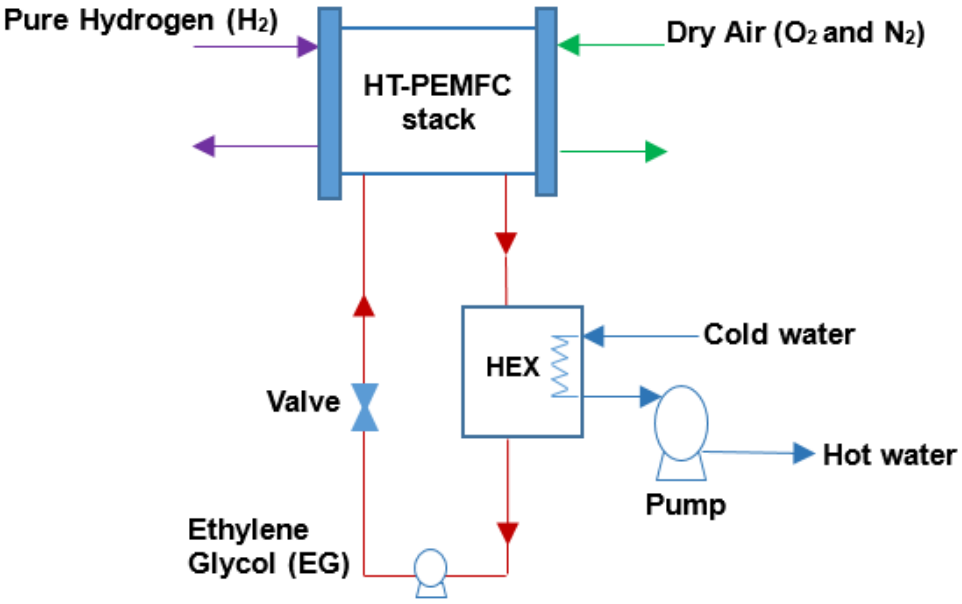

Figure 4.2 Schematic diagram of the simple cogeneration system

Table 4.3 Operating parameters of the cogeneration system

Parameters	**Value**
Current density (i) at 0.6 V	0.42 A/cm^2
Active Area (A_{cell})	150 cm^2
Number of cells (N_{cell})	13
Mass flow rate of coolant ($\dot{m}_{coolant}$)	0.019 kg/s
Specific heat capacity of coolant ($c_{p,coolant}$)	2.84 kJ/kg-K
Anode and cathode temperatures (T_a, T_c)	160 °C
Inlet temperature of coolant ($T_{1,EG}$)	95 °C

4.3.1 HT-PEMFC stack

The details of the one dimensional and semi-empirical model for a HT-PEMFC is mentioned above in the Section 4.2. Only H_2 and O_2 are the reactant gases, and N_2 is the inert gas, in the HT-PEMFC stack. The single cell voltage (E_{cell}) can be calculated Eq. (4.28). The activation losses for the anode and cathode are shown in Eqs. (4.31) and (4.32), respectively. The total ohmic losses for both proton and electron transfer are calculated as shown in Eq. (4.36).

It is assumed that each cell in the stack has the same performance. Thus, the stack voltage (E_{stack}) can be obtained multiplying the cell voltage with the number of cells (N_{cell}), as shown in Eq. (4.38); and the power density ($\dot{W}_{FC}^{"}$) of the stack can be found multiplying the current density with stack voltage, as shown in Eq. (4.40).

$$E_{stack} = N_{cell} \cdot E_{cell} \tag{4.38}$$

$$\dot{W}_{FC}^{"} = i \cdot E_{stack} \tag{4.40}$$

Figure 4.3 shows the control volume used in the energy balance for the HT-PEMFC stack. The energy balance around the control volume is applied to find the outlet temperature of coolant. Here, HT-PEMFC stack is assumed to be adiabatic.

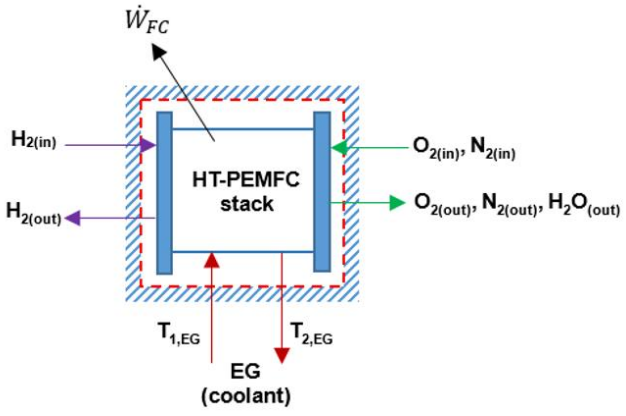

Figure 4.3 The control volume used in the energy balance of the HT-PEMFC stack

The energy balance equation in the stack is given as follows;

$$0 = \sum\left(\dot{n}_i^{"}\bar{h}_i\right)_{in} - \sum\left(\dot{n}_i^{"}\bar{h}_i\right)_{out} - \dot{W}_{FC}^{"} + \sum\left(\dot{n}_{EG}^{"}\bar{h}_{EG}\right)_{in} - \sum\left(\dot{n}_{EG}^{"}\bar{h}_{EG}\right)_{out} \quad (4.41)$$

The molar flow rates of species in the HT-PEMFC stack are calculated using Faraday's Law and are showed in the Table 4.4.

Table 4.4 Molar flow rate of chemical species

Inlet molar flow rates of species	**Outlet molar flow rates of species**
$\dot{n}_{H_{2,in}}^{"} = \lambda_{H_2} \cdot \frac{i}{2 \cdot F} \cdot N_{cell}$	$\dot{n}_{H_{2,out}}^{"} = (\lambda_{H_2} - 1) \cdot \frac{i}{2 \cdot F} \cdot N_{cell}$
$\dot{n}_{O_{2,in}}^{"} = \lambda_{O_2} \cdot \frac{i}{4 \cdot F} \cdot N_{cell}$	$\dot{n}_{O_{2,in}}^{"} = (\lambda_{O_2} - 1) \cdot \frac{i}{4 \cdot F} \cdot N_{cell}$
$\dot{n}_{N_{2,in}}^{"} = \frac{X_{N_2}}{X_{O_2}} \dot{n}_{O_{2,in}}^{"}$	$\dot{n}_{N_{2,out}}^{"} = \dot{n}_{N_{2,in}}^{"}$
$\dot{n}_{H_2O,in}^{"} = 0$	$\dot{n}_{H_2O,out}^{"} = \dot{n}_{H_2O,gen}^{"} = \frac{i}{2 \cdot F} \cdot N_{cell}$

To calculate the outlet temperature of coolant ($T_{2,EG}$), Eq. (4.41) can be rewritten as shown in Eq. (4.42).

$$0 = \left(\dot{n}_{H_{2,in}}^{"}\bar{h}_{H_2} + \dot{n}_{O_{2,in}}^{"}\bar{h}_{O_2} + \dot{n}_{N_{2,in}}^{"}\bar{h}_{N_2}\right) - \left(\dot{n}_{H_{2,out}}^{"}\bar{h}_{H_2} + \dot{n}_{O_{2,out}}^{"}\bar{h}_{O_2} + \dot{n}_{N_{2,out}}^{"}\bar{h}_{N_2} + \dot{n}_{H_2O,out}^{"}\bar{h}_{H_2O}\right) + \dot{n}_{coolant}^{"}\bar{c_p}_{coolant}(T_{2,EG} - T_{1,EG}) - \dot{W}_{FC}^{"} \quad (4.42)$$

4.3.2 Heat exchanger

Figure 4.4 shows the heat exchanger and fluids in the inside. This heat exchanger is used to cool ethylene glycol used in the fuel cell stack and to heat the network water. According to the calculations, the temperature of ethylene glycol increases 10°C while it cools HT-PEMFC stack, thus the temperature of ethylene glycol at the fuel cell outlet is 105°C. This result is confirmed with experimental results. The outlet temperature of hot water can be calculated using the energy balance shown in Eq. (4.43).

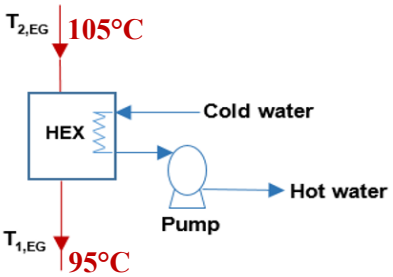

Figure 4.4 The heat exchanger in the simple cogeneration system

$$T_{W,out} = T_{W,in} + \frac{\dot{n}^{"}_{coolant}\overline{c_p}_{coolant}(T_{2,EG}-T_{1,EG})}{\dot{n}^{"}_{water}\overline{c_p}_{water}} \quad (4.43)$$

4.3.3 System modeling

To assess the performance of the HT-PEMFC stack based cogeneration system, the electrical efficiency and the fuel utilization efficiency are selected. The electrical efficiency ($\eta_{electrical}$) is calculated by dividing the fuel cell power output to the chemical energy of hydrogen supplied to the cogeneration system. The fuel utilization efficiency (FUE) is defined as the ratio between the total amounts of useful energy to the chemical energy of hydrogen.

$$\eta_{electrical,simplecogen} = \frac{\dot{W}_{FC}}{\dot{n}^{"}_{H_{2,in}}\cdot\overline{LHV}_{H_2}} \quad (4.44)$$

$$FUE = \frac{\dot{W}_{FC}+\dot{n}^{"}_{water}\overline{c_p}_{water}(T_{W,out}-T_{W,in})}{\dot{n}^{"}_{H_{2,in}}\cdot\overline{LHV}_{H_2}} \quad (4.45)$$

4.4 The thermodynamic model for a cogeneration system (including HT-PEMFC, SMR, WGS, and burner) that converts natural gas into electricity and heat

In this section, the energy and exergy analyses of the cogeneration system including the fuel processing system, HT-PEMFC power system, and auxiliary components are presented in detail. This modeling equations are calculated using EES software. The effects of steam-to-carbon ratio, operating cell temperature, and anode stoichiometric ratio on the performance of the cogeneration system (electrical efficiency and

cogeneration efficiency) are investigated in the energy analysis. In the exergy analysis, the exergy destructions of each component are calculated. In addition, the effect of steam-to-carbon ratio, operating cell temperature, and anode stoichiometric ratio on the exergetic efficiency of cogeneration system and exergy destruction of each component in the system are investigated.

The HT-PEMFC based cogeneration system (including HT-PEMFC, SMR, WGS, and catalytic burner) is shown schematically in Figure 4.5. This cogeneration system includes fuel processing system (SMR, WGS, and catalytic burner), HT-PEMFC stack, and auxiliary components (water pump, compressor, air blower, and heat exchangers). As shown in Figure 4.5, water is pumped to the steam generator and here it is heated using the gas mixture at the outlet of the SMR. The heated steam and the methane gas from the compressor are mixed in the mixer and this steam-fuel mixture is fed to the SMR reactor. The catalytic burner is fed with dry air and the exhaust reformate gases from the anode outlet of the HT-PEMFC. As a result of the chemical reaction occurring inside the burner, hot gas mixture produces, which provides the necessary heat for the endothermic reaction in the SMR reactor. The reformate gas formed in the SMR reactor reacts with water in the water-gas-shift reactor (WGS) to reduce the CO ratio to an acceptable level for the fuel cell. The reformate gas is supplied from anode to fuel cell; whereas the dry air is supplied from cathode to fuel cell. The reformate gas includes H_2, CO, CH_4, CO_2, and H_2O; whereas air includes O_2 and N_2. Thus, the electrochemical reaction occurs in the fuel cell and the chemical energy is converted directly into electrical energy. The fuel cell which operates at high temperature is cooled with ethylene glycol (EG). Hot EG passes through the Heat Exchanger-4 (HEX-4) shown in Figure 4.5 to heat the water. This water is heated again with the hot exhaust gas at the outlet of the cathode in the Heat Exchanger-3 (HEX-3) and after that it is heated with hot flue gas at the outlet of steam generator. Then, this network water is heated with reformate gas in the Heat Exchangers-1 and 2 (HEX-1 and HEX-2), respectively. Thus, hot water is produced using several heat exchangers in the cogeneration system.

General assumptions used in the modeling of the integrated cogeneration system are as follows:

- The system and components are in steady state operation.
- Natural gas is taken as methane (CH_4).
- Complete burning occurs in the catalytic burner.
- Dry air (21% O_2 and 79% N_2) is fed to the air blower.
- None of the reactants in the fuel cell are in liquid phase.
- Kinetic and potential energy are neglected in the energy balances.
- All component in the system are assumed to be thermally insulated.

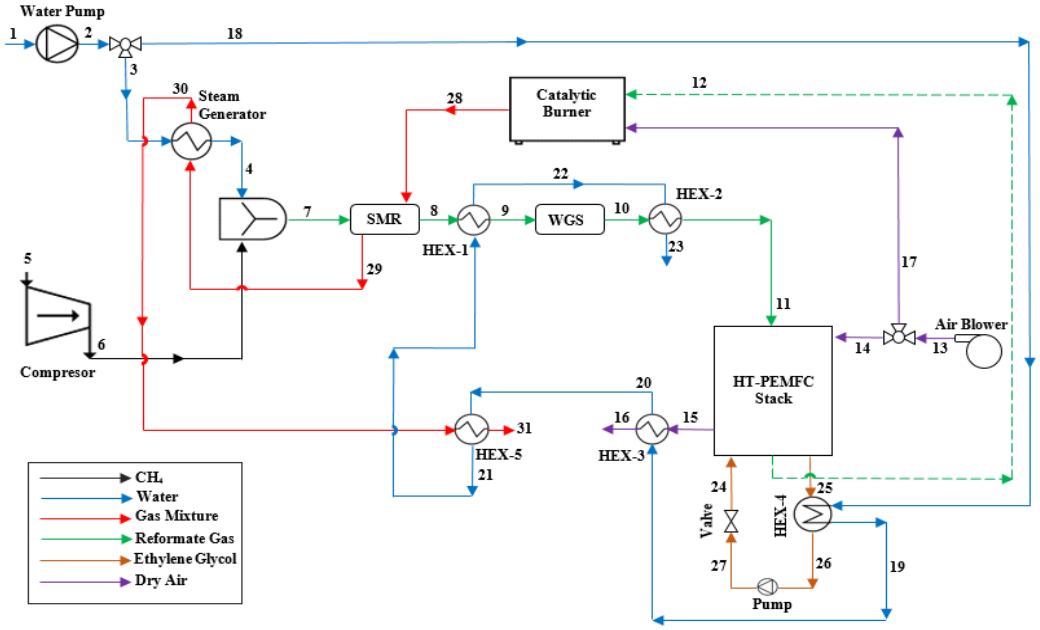

Figure 4.5 The HT-PEMFC based cogeneration system

4.4.1 Energy analysis of HT-PEMFC based cogeneration system

In this section, the energy analysis of each component is presented. The operating parameters of the HT-PEMFC and the input parameters of the cogeneration system are shown in Table 4.5.

4.4.1.1 HT-PEMFC stack

The development of the one-dimensional and semi-empirical model of HT-PEMFC is presented in Section 4.2; and the HT-PEMFC stack modeling is explained in Section 4.3.1. In this integrated cogeneration system, dry air (O_2 and N_2) is fed from the cathode while the reformate gas (CH_4, H_2, CO_2, CO and H_2O) is fed from the anode side of the HT-PEMFC stack. H_2 and O_2 are the reactant gases entering the global fuel cell reaction. Other chemical species found in the fuel and oxygen streams act as inert gases.

Table 4.5 The operating parameters of the HT-PEMFC and the input parameters of the cogeneration system

HT-PEMFC	
Parameters	**Value**
Cell Voltage, E_{cell}	0.6 V
Number of Cells, N_{cell}	36
Active Area, A_{active}	150 cm^2
Anode Stoichiometry Ratio, λ_a	1.2
Cathode Stoichiometry Ratio, λ_c	2.5
Membrane	Polybenzimidazole (PBI)
Cell Temperature, T_{cell}	160°C
Inlet Temperature of Air in the Fuel Cell	25°C
Coolant	Ethylene Glycol
Inlet Temperature of Coolant	95°C
COGENERATION SYSTEM	
Parameters	**Value**
Inlet Temperature of Network Water for January in Ankara	25°C
Inlet Temperature of Reformate Gas in the SMR	125°C
Inlet Temperature of Reformate Gas in the WGS	250°C
Catalyst Type of Steam Reforming	Ni-Al_2O_3
Catalyst Type of High Temperature Shift (HTS)	SHT-4
Catalyst Type of Low Temperature Shift (LTS)	MDC-7
Temperature Range for HTS	400-600 °C
Temperature Range for LTS	200-300 °C

4.4.1.2 Fuel processing system

A typical fuel processing system includes a steam-methane reformer (SMR), a water gas shift reactor (WGS), and a catalytic burner. Initially, the SMR reactor is fed with CH_4 and H_2O, while the catalytic burner is fed with dry air and anode exhaust gases. The hot flue gas which is produced in the catalytic burner is supplied to the SMR reactor for endothermic reaction. Although there are ten chemical reactions in

the fuel processing system (Xu and Froment, 1989), three chemical reactions have been dealt with in this model to simplify calculations. These chemical equations are as follows;

Methane Steam Reforming:

$$CH_4 + H_2O \leftrightarrow CO + 3H_2 \qquad \Delta\bar{h}_1 = 206{,}000\, J/mol \tag{4.46}$$

Water Gas Shift:

$$CO + H_2O \leftrightarrow CO_2 + H_2 \qquad \Delta\bar{h}_2 = -41{,}000\, J/mol \tag{4.47}$$

Direct Steam Reforming:

$$CH_4 + 2H_2O \leftrightarrow CO_2 + 4H_2 \qquad \Delta\bar{h}_3 = 165{,}000\, J/mol \tag{4.48}$$

where, $\Delta\bar{h}_i$ represents the specific enthalpy changes of chemical reactions (i: 1, 2, 3 for methane steam reforming, water gas shift, and direct steam reforming, respectively). The reaction rates of chemical reactions occurring in the SMR reactor and the WGS reactor are calculated in Eqs. (4.49)-(4.51) (Xu and Froment, 1989).

$$r_1 = A_1 exp\left(\frac{-E_1}{\bar{R}T}\right)\left(P_{CH_4}P_{H_2O} - \frac{P_{H_2}^3 P_{CO}}{K_{p,1}}\right)/\left(P_{H_2}^{2,5}\cdot DEN^2\right) \tag{4.49}$$

$$r_2 = A_2 exp\left(\frac{-E_2}{\bar{R}T}\right)\left(P_{CO}P_{H_2O} - \frac{P_{H_2}P_{CO}}{K_{p,2}}\right)/\left(P_{H_2}\cdot DEN^2\right) \tag{4.50}$$

$$r_3 = A_3 exp\left(\frac{-E_3}{\bar{R}T}\right)\left(P_{CH_4}P_{H_2O}^2 - \frac{P_{H_2}^4 P_{CO_2}}{K_{p,3}}\right)/\left(P_{H_2}^{3,5}\cdot DEN^2\right) \tag{4.51}$$

where, A_i, $K_{p,i}$ and E_i are defined as the pre-exponential factor, the equilibrium constant and the activation energy for the i reaction, respectively. P_j is defined as partial pressures of the species (j: CH_4, CO, H_2, CO_2, H_2O) in the reaction. Finally, DEN specifies the adsorption of reacting species to the active catalyst sites. DEN is calculated as follows;

$$DEN = 1 + K_{CH_4}P_{CH_4} + K_{CO}P_{CO} + K_{H_2}P_{H_2} + K_{H_2O}\frac{P_{H_2O}}{P_{H_2}} \tag{4.52}$$

where, K_j is defined as the adsorption constant of species j on the catalyst ($Ni/MgAl_2O_4$) and is calculated using Van't Hoff equation given below (Xu and Froment, 1989).

$$K_j = K_{j,0} \cdot exp\left(\frac{-\Delta\bar{h}_j}{\bar{R}T}\right) \tag{4.53}$$

According to the three chemical reactions given in Eqs. (4.54)-(4.58), the molar flow rate balance equations for CH_4, CO, CO_2, H_2O, and H_2 are calculated for the SMR.

$$\dot{n}_{CH_4}^{SMR,out} = \dot{n}_{CH_4}^{SMR,in} - (r_1 + r_3) \tag{4.54}$$

$$\dot{n}_{H_2O}^{SMR,out} = \dot{n}_{H_2O}^{SMR,in} - (r_1 + r_2 + 2r_3) \tag{4.55}$$

$$\dot{n}_{H_2}^{SMR,out} = 3r_1 + r_2 + 4r_3 \tag{4.56}$$

$$\dot{n}_{CO_2}^{SMR,out} = r_2 + r_3 \tag{4.57}$$

$$\dot{n}_{CO}^{SMR,out} = r_1 - r_2 \tag{4.58}$$

The hydrogen-rich reformate gas from SMR reactor reaches to the WGS reactor. The aim of WGS reactor is to reduce the content of CO and increase H_2 content in the reformate gas (Arsalis et al., 2012). The WGS reactor includes high temperature shift (HTS) and low temperature shift (LTS), and the exothermic reaction (Eq. (4.47)) occurs in the WGS reactor. The reformate gas enters in the HTS, and then in the LTS. Therefore, the molar flow rate balance equations for species are expressed as follows:

$$\dot{n}_{CH_4}^{WGS,out} = \dot{n}_{CH_4}^{SMR,out} \tag{4.59}$$

$$\dot{n}_{H_2O}^{WGS,out} = \dot{n}_{H_2O}^{SMR,outlet} - (r_{2,HTS} + r_{2,LTS}) \tag{4.60}$$

$$\dot{n}_{H_2}^{WGS,out} = \dot{n}_{H_2}^{SMR,outlet} + (r_{2,HTS} + r_{2,LTS}) \tag{4.61}$$

$$\dot{n}_{CO_2}^{WGS,out} = \dot{n}_{CO_2}^{SMR,out} + (r_{2,HTS} + r_{2,LTS}) \tag{4.62}$$

$$\dot{n}_{CO}^{WGS,out} = \dot{n}_{CO}^{SMR,out} - (r_{2,HTS} + r_{2,LTS}) \quad (4.63)$$

In the above equations, $r_{2,HTS}$ and $r_{2,LTS}$ show the reaction rates for the HTS and LTS, respectively. Tables 4.6 and 4.7 show all parameters related to reaction kinetics, equilibrium constants, and adsorption constants for SMR and WGS (HTS and LTS).

The SMR reactor, the WGS reactor, and the catalytic combustor are thermodynamically modeled using the following equation together with the above chemical equations. It should be noted that these components are assumed to be thermally insulated.

$$\left(\sum_i^k \dot{n}[i] \cdot \bar{h}_i\right)_{in} = \left(\sum_i^k \dot{n}[i] \cdot \bar{h}_i\right)_{out} \quad (4.64)$$

Table 4.6 The parameters of reaction kinetics and the equilibrium constants

Reaction Number, i	**Pre-exponential Factor, A_i**	**Ref.**	**Activation Energy, J/mol**	**Ref.**	**Equilibrium Constant, Kp_i**	**Ref.**
1	$2.084 \cdot 10^{13}$ kmol·bar$^{0.5}$/(kg·h)	(Oliveira et al., 2009)	2170010 J/mol	(Oliveira et al., 2009)	$1.198 \cdot 10^{13} \cdot \exp(-26830/T)$ bar^2	(Hou and Hughes, 2001)
2	$3.359 \cdot 10^{7}$ kmol·bar^{1}/(kg·h)	(Oliveira et al., 2009)	68200 J/mol	(Oliveira et al., 2009)	$1.767 \cdot 10^{-2} \cdot \exp(4400/T)$	(Hou and Hughes, 2001)
3	$4.644 \cdot 10^{13}$ kmol·bar$^{0.5}$/(kg·h)	(Oliveira et al., 2009)	215840 J/mol	(Oliveira et al., 2009)	$2.117 \cdot 10^{11} \cdot \exp(-22430/T)$ bar^2	(Hou and Hughes, 2001)
HTS	$1.78 \cdot 10^{22} \cdot (1+0.0097 \cdot SCR - 1.1364 \cdot SCR^2) \cdot T^{-8}$	(Chen et al., 2008)	70000 J/mol	(Chen et al., 2008)	-	-
LTS	$1.74 \cdot 10^{17} \cdot (1-0.1540 \cdot SCR - 0.0008 \cdot SCR^2) \cdot T^{-8.5}$	(Chen et al., 2008)	35000 J/mol	(Chen et al., 2008)	-	-

Table 4.7 Constants in Van't Hoff equation

Species	**Pre-exponential Factor, $K_{j,0}$**	**Adsorption Specific Entalpy, $\Delta\bar{h}_j$, J/mol**	**Adsorption Constant, K_j**
CH_4	6.65 x 10^{-4} bar^{-1}	-38,280	0.1791 bar^{-1}
CO	8.23 x 10^{-5} bar^{-1}	-70,650	40.91 bar^{-1}
H_2	6.12 x 10^{-9} bar^{-1}	-82,900	0.0296 bar^{-1}
H_2O	1.77 x 10^{5} bar^{0}	88,680	0.4152 bar^{0}

In the catalytic burner, dry air (O_2 and N_2) and anode exhaust gases (CH_4, CO, H_2, CO_2, H_2O) react to produce hot flue gases. It has been accepted that complete combustion occurs in the catalytic burner. The chemical reaction occurring in the catalytic burner is shown in Eq. (4.65).

$$CH_4 + a \cdot H_2 + b \cdot CO_2 + c \cdot CO + d \cdot H_2O + \alpha(O_2 + 3{,}76N_2) \rightarrow x \cdot CO_2 + y \cdot H_2O + z \cdot N_2 \quad (4.65)$$

4.4.1.3 Heat exchangers

In the current cogeneration system five heat exchangers and steam generator are used. All flows are unmixed. These heat exchangers fulfill the following tasks for the cogeneration system:

- Water preheater (Steam generator): The steam generator (SG) consists of three parts: an economizer, an evaporator and a superheater. The water sent from the water pump is pumped to the economizer and the hot flue gas at the outlet of the SMR reactor enters the steam generator in the reverse direction to heat the water, before mixing with CH_4 in the mixer.
- Reformate gas heater (HEX-1): It is located between SMR reactor and WGS reactor. In the heat exchanger, reformate gas from SMR reactor is used to heat water from HEX-5.
- Reformate gas cooler (HEX-2): It is located between WGS reactor and condenser. This is essential so that the reformate gas is at a low temperature (160°C) before reaching the condenser and HT-PEMFC stack. Reformate gas from WGS reactor is cooled while water is heated.
- Water preheater (HEX-3): It is located at the cathode outlet of HT-PEMFC stack. The cathode exhaust gases are used to heat water.
- Ethylene glycol cooler (HEX-4): It is used to refrigerate ethylene glycol for HT-PEMFC stack. At the same time, the water is heated.
- Hot flue gas cooler (HEX-5): The hot flue gas used in steam generator heats water in the HEX-5.

In Table 4.8, the energy balance equations for each heat exchangers are given together with the hot and cold fluid streams used in these heat exchangers. All heat exchangers are used to heat up the water coming from domestic water supply and also to cool the hot fluid passing through it.

Table 4.8 Heat exchangers and energy balances

HEX No.	Hot Fluid	Cold Fluid	Energy Balance
HEX-1	Reformate Gas	Water	$\dot{n}_8 \cdot \bar{h}_8 - \dot{n}_7 \cdot \bar{h}_7 = \dot{n}_{22} \cdot \bar{h}_{22} - \dot{n}_{21} \cdot \bar{h}_{21}$
HEX-2	Reformate Gas	Water	$\dot{n}_{10} \cdot \bar{h}_{10} - \dot{n}_{11} \cdot \bar{h}_{11} = \dot{n}_{23} \cdot \bar{h}_{23} - \dot{n}_{22} \cdot \bar{h}_{22}$
HEX-3	Anode Exhaust Gas	Water	$\dot{n}_{15} \cdot \bar{h}_{15} - \dot{n}_{16} \cdot \bar{h}_{16} = \dot{n}_{20} \cdot \bar{h}_{20} - \dot{n}_{19} \cdot \bar{h}_{19}$
HEX-4	Ethylene Glycol	Water	$\dot{n}_{25} \cdot \bar{h}_{25} - \dot{n}_{26} \cdot \bar{h}_{26} = \dot{n}_{19} \cdot \bar{h}_{19} - \dot{n}_{18} \cdot \bar{h}_{18}$
HEX-5	Hot Flue Gas	Water	$\dot{n}_{31} \cdot \bar{h}_{31} - \dot{n}_{30} \cdot \bar{h}_{30} = \dot{n}_{21} \cdot \bar{h}_{21} - \dot{n}_{20} \cdot \bar{h}_{20}$

4.4.1.4 Performance assessment parameters of the integrated systems

The performance of the system is discussed in terms of efficiency (electrical and cogeneration). The electrical efficiency of the system ($\eta_{electrical}$) is defined as the ratio of the net electrical power output of the system to the chemical energy of the fuel entering the system, as shown in Eq. (4.66). The cogeneration efficiency of the system ($\eta_{cogeneration}$) is defined as the ratio of the sum of the waste heat recovered by the heat exchangers and the net electrical power to the chemical energy of the fuel entering the system, as shown in Eq. (4.67).

$$\eta_{electrical} = \frac{\dot{W}_{net\_electrical}}{\dot{n}_{CH_4,input} \cdot \overline{LHV}_{CH_4}} \tag{4.66}$$

$$\eta_{cogeneration} = \frac{\dot{W}_{net\_electrical} + \dot{Q}_{HEX,cogen}}{\dot{n}_{CH_4,input} \cdot \overline{LHV}_{CH_4}} \tag{4.67}$$

where $\overline{LHV}_{CH_4}$ is Lower Heating Value of CH_4. The net electrical power ($\dot{W}_{net\_electrical}$) is calculated by subtracting the power consumed in the system ($\dot{W}_{pump} + \dot{W}_{comp} + \dot{W}_{blower}$) from the power generated from the fuel cell ($\dot{W}_{fuelcell}$).

$$\dot{W}_{net\_electrical} = \dot{W}_{fuelcell} - (\dot{W}_{pump} + \dot{W}_{comp} + \dot{W}_{blower}) \tag{4.68}$$

The waste heat recovered by the heat exchangers ($\dot{Q}_{HEX,cogen}$) is the sum of the waste heat rates from each heat exchanger.

$$\dot{Q}_{HEX,cogen} = \dot{Q}_{HEX,1} + \dot{Q}_{HEX,2} + \dot{Q}_{HEX,3} + \dot{Q}_{HEX,4} + \dot{Q}_{HEX,5} \quad (4.69)$$

4.4.2 Exergy analysis of HT-PEMFC based cogeneration system

In this section, the equations used for exergy analysis in the cogeneration system is given. Exergy is defined as the maximum work ability between the system and the environmental using thermodynamics laws. Unlike energy, exergy cannot be conserved but can be destroyed. In addition, while energy deals only with the amount of energy, exergy deals with both quantity and quality of energy (Kazim, 2004).

The total exergy consists of the physical exergy ($\overline{ex}_i^{PH}$) and the chemical exergy ($\overline{ex}_i^{CH}$). The exergy of a flowing stream *i* can be calculated as follows,

$$\overline{ex}_i = \overline{ex}_i^{PH} + \overline{ex}_i^{CH} \quad (4.70)$$

4.4.2.1 Physical exergy

The physical exergy is related to the temperature and pressure of the species. The physical flow exergy is calculated using Eq. (4.71).

$$\overline{ex}_i^{PH} = \left(\bar{h}_i - \bar{h}_0\right) - T_0 \cdot (\bar{s}_i - \bar{s}_0) \quad (4.71)$$

where $\bar{h}$ and $\bar{s}$ are the specific enthalpy and entropy of species, respectively, and T_0 is the reference temperature (K). The subscript 0 shows for the value of property at the condition of the reference environment (the reference temperature of 298.15 K and the reference pressure of 101.325 kPa). The values of enthalpy ($\bar{h}_0$) and entropy ($\bar{s}_0$) at the reference environmental are given in the Table 4.9.

Table 4.9 The reference specific enthalpy and entropy values at the 298.15 K and 101.325 kPa

Species, j	**Specific Enthalpy, $\bar{h}_0$ (kJ/kmol)**	**Specific Entropy, $\bar{s}_0$ (kJ/kmol-K)**
CH_4	-74,595	186.3
H_2	0	130.6
H_2O	-241,811	188.7
CO	-110,528	197.5
CO_2	-393,486	213.7
O_2	0	205
N_2	0	191.5

4.4.2.2 Chemical exergy

The chemical exergy is related to chemical composition of a system. Chemical flow exergy of species for ideal gas mixtures is calculated using Eq. (4.72).

$$\bar{ex}_i^{CH} = \sum X_j \cdot \bar{ex}_j^{CH} + \bar{R} \cdot T_0 \cdot \sum X_j \cdot \ln(X_j) \qquad (4.72)$$

where X_j is the mole fraction of the species j in the system, $\bar{ex}_j^{CH}$ is the chemical exergy of species j in the system at the reference environment. These chemical exergies of species at the reference environmental are presented in Table 4.10.

Table 4.10 The chemical exergy values of species at the 298.15 K and 101.325 kPa (Moran et al., 2010)

Species, j	**Standard Chemical Exergy, $\overline{ex}_j^{CH}$ (kJ/kmol)**
CH_4	824,350
H_2	235,250
H_2O	8,635
CO	269,410
CO_2	14,175
O_2	3,950
N_2	640

4.4.2.3 Exergy balance

An exergy balance is generally applied to a control volume to find the exergy destructions within that volume. The calculation steps for exergy analysis are given as follows:

- The physical exergy flow rates for all states in the system are calculated.
- The chemical exergy flow rates for all states in the system are calculated.
- Several control volumes in the cogeneration system are defined.
- Exergy balance equations are used to find the exergy destruction rates of each component.
- The exergetic efficiency of the cogeneration system is calculated.

The general form of the steady state control volume exergy balance is given as follows;

$$0 = \sum_j \dot{E}_{Q,j} - \dot{W}_{cv} + \sum_i \dot{Ex}_i - \sum_e \dot{Ex}_e - \dot{Ex}_D \tag{4.73}$$

where

$$\dot{E}_{Q,j} = \left(1 - \frac{T_0}{T_j}\right) \cdot Q_j \tag{4.74}$$

$$\dot{Ex}_i = \dot{n}_i \cdot \overline{ex}_i \tag{4.75}$$

$$\dot{Ex}_e = \dot{n}_e \cdot \overline{ex}_e \tag{4.76}$$

where $\overline{ex}_i$ and $\overline{ex}_e$ are defined as the specific molar exergy of input and output species. $\dot{Ex}_D$ is the exergy destruction rate in the control volume of system. $\dot{E}_{Q,j}$ is neglected in the calculations. The control volumes and the exergy balance equations of each component are shown in Table 4.11.

The ratio between the exergy destruction rate of a component and the exergy rate of the fuel supplied to cogeneration system (y_D) is calculated using Eq. (4.77). The

ratio between the exergy destruction rate of a component and the total exergy destruction rate (y_D^*) is calculated using Eq. (4.78).

$$y_D = \frac{\dot{Ex}_D}{\dot{Ex}_{fuel}} \tag{4.77}$$

$$y_D^* = \frac{\dot{Ex}_D}{\dot{Ex}_{D,total}} \tag{4.78}$$

4.4.2.3 Performance assessment parameters

The product and the fuel for the cogeneration system are necessary to define the exergetic efficiency. In this cogeneration system, the product is the net electrical power output of the cogeneration system and the beneficial heat to produce hot water; whereas the fuel is CH_4 entering the system. Therefore, the exergetic efficiency is calculated using Eq. (4.79).

$$\varepsilon_{ex} = \frac{\dot{W}_{net\_electrical} + \dot{Ex}_{hotwater}}{\dot{n}_{CH_4,input} \cdot \overline{ex}_{CH_4}} \tag{4.79}$$

where

$$\dot{Ex}_{hotwater} = \dot{n}_{14} \cdot (\overline{ex}_{24} - \overline{ex}_{19}) \tag{4.80}$$

Table 4.11 Control volume and exergy balance equations of all components

Components	**Control Volume**	**Exergy Balance**
Water Pump	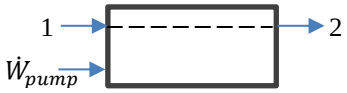	$\dot{W}_{pump} + \dot{E}x_1 - \dot{E}x_2 - \dot{E}x_{D,pump} = 0$
Compressor	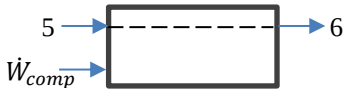	$\dot{W}_{comp} + \dot{E}x_5 - \dot{E}x_6 - \dot{E}x_{D,comp} = 0$
Mixer	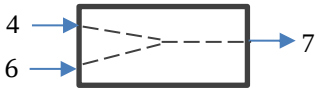	$\dot{E}x_4 + \dot{E}x_6 - \dot{E}x_7 - \dot{E}x_{D,mixer} = 0$
SMR	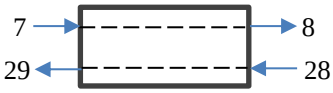	$\dot{E}x_7 + \dot{E}x_{28} - \dot{E}x_8 - \dot{E}x_{29} - \dot{E}x_{D,SMR} = 0$
WGS		$\dot{E}x_9 - \dot{E}x_{10} - \dot{E}x_{D,WGS} = 0$
Catalytic Burner		$\dot{E}x_{12} + \dot{E}x_{17} - \dot{E}x_{28} - \dot{E}x_{D,burner} = 0$
HT-PEMFC Stack	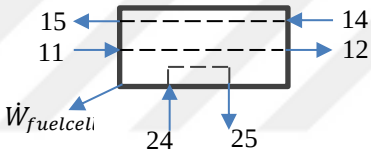	$\dot{E}x_{14} + \dot{E}x_{11} + \dot{E}x_{24} - \dot{E}x_{15} - \dot{E}x_{12} - \dot{E}x_{25} - \dot{W}_{fuelcell} - \dot{E}x_{D,fuelcell} = 0$
HEX-1	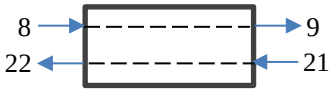	$\dot{E}x_7 + \dot{E}x_{28} - \dot{E}x_8 - \dot{E}x_{29} - \dot{E}x_{D,HEX1} = 0$
HEX-2	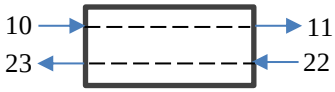	$\dot{E}x_{10} + \dot{E}x_{22} - \dot{E}x_{11} - \dot{E}x_{23} - \dot{E}x_{D,HEX2} = 0$
HEX-3	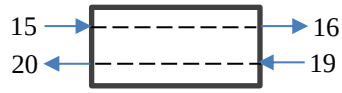	$\dot{E}x_{15} + \dot{E}x_{19} - \dot{E}x_{16} - \dot{E}x_{20} - \dot{E}x_{D,HEX3} = 0$
HEX-4	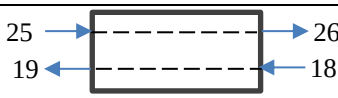	$\dot{E}x_{25} + \dot{E}x_{18} - \dot{E}x_{26} - \dot{E}x_{19} - \dot{E}x_{D,HEX4} = 0$
HEX-5	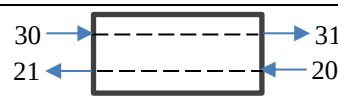	$\dot{E}x_{30} + \dot{E}x_{20} - \dot{E}x_{31} - \dot{E}x_{21} - \dot{E}x_{D,HEX-5} = 0$

CHAPTER FIVE
RESULTS AND DISCUSSION

5.1 Introduction

In this chapter, the results and discussion of the modeling and experimental studies are presented in different subsections. Firstly, the experimental results of Chapter 3 are given for different binder (PBI and PVDF), operating cell temperature, and Pt loadings. After that, the calibration of some modeling parameters for the one-dimensional and semi-empirical model of HT-PEMFC using Genetic Algorithm are explained. In addition, the effect of binder on the performance of the fuel cell is examined. Then, the effects of operating temperature, Pt loadings, and percentage of phosphoric acid on the performance of the fuel cell are investigated for HT-PEMFC models for both PBI and PVDF binders. The effect of anode stoichiometry ratio on the performance of the HT-PEMFC stack based simple cogeneration system is studied and the average temperatures of the hot water for each month for Ankara province are calculated for household applications (e.g. shower, dishwasher, and washing machine). Finally, the effect of some parameters on the performance of the integrated cogeneration system (including HT-PEMFC, SMR, WGS, and burner) are investigated. In addition, the results of energy and exergy analyses are given for each component in the system.

5.2 Experimental study

The experimental study includes the effect of the different operating cell temperatures (160°C, 180°C, and 200°C), Pt loadings (0.6 mg/cm^2, 1 mg/cm^2, and 1.5 mg/cm^2), and binders (PBI and PVDF) on the performance of the fuel cell.

5.2.1 The effect of different operating cell temperature

Figure 5.1 shows the polarization curves obtained from the experimental study for different operating cell temperature (160°C, 180°C, and 200°C) for 1 mg/cm^2 and

PVDF binder. When the cell temperature increases, the rate of reaction kinetics and the proton conductivity of the PBI membrane increase. Thus, when the operating cell temperature increases, the cell voltage and power density increase, as can be seen from this figure. The increase of power density at 0.6 V is found to be 55% when the cell temperature is increased from 160°C to 200°C. However, high operating cell temperature might affect negatively the materials and start-up time of the fuel cell.

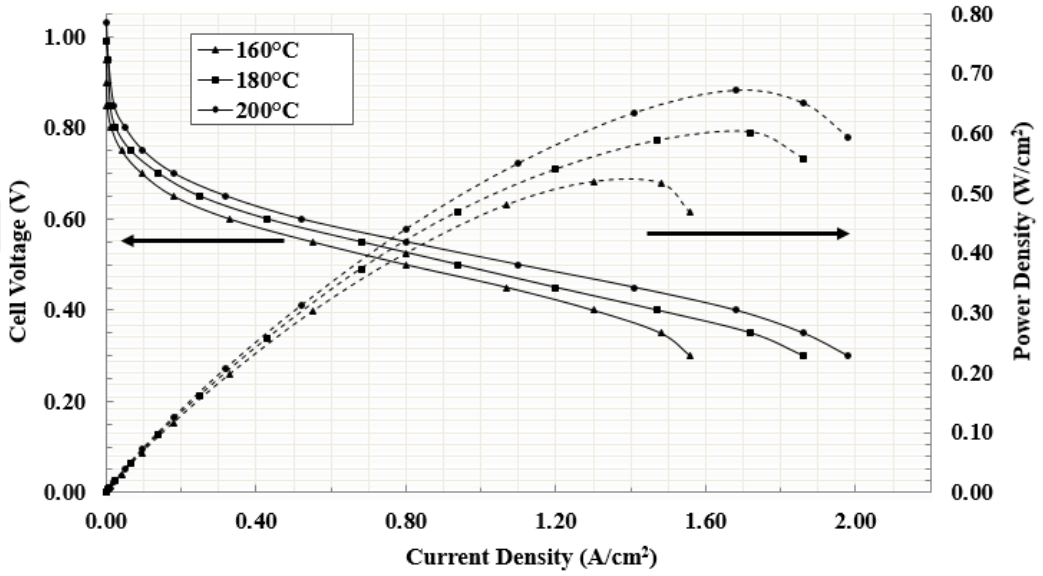

Figure 5.1 The polarization curves of experimental study for different operating cell temperature

5.2.2 The effect of different Pt loadings

Figure 5.2 shows the polarization curves of experimental study for different Pt loadings (0.6 mg/cm^2, 1 mg/cm^2, and 1.5 mg/cm^2) for 160°C and PVDF binder. Thin film thicknesses on the anode and cathode catalyst layer decrease with increasing Pt loadings. Thin film thickness affects negatively the performance of the fuel cell and it will be given in detail in Section 5.3.3.2. Thus, when the Pt loadings increase, the cell voltage and power density increase, as can be seen from this figure. The power densities at 0.6 V were calculated as 0.14 W/cm^2 (for 0.6 mg/cm^2 Pt loading), 0.20 W/cm^2 (for 1 mg/cm^2 Pt loading), and 0.25 W/cm^2 (for 1.5 mg/cm^2 Pt loading).

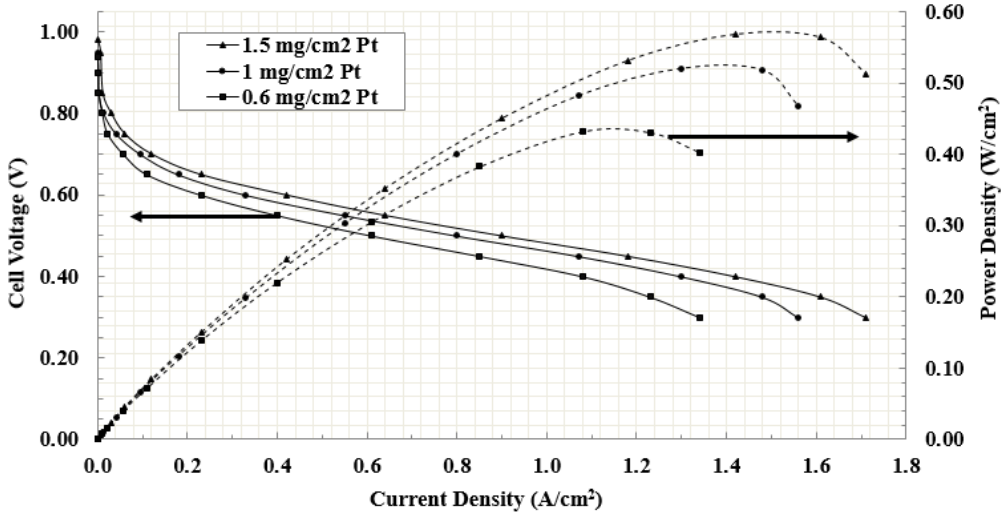

Figure 5.2 The polarization curves of experimental study for different Pt loadings

5.2.3 The effect of different binders

Figure 5.3 shows the polarization curves of experimental study for different binders (PBI and PVDF) for 160°C and 1.5 mg/cm^2. PBI binder has hydrophilic nature while, PVDF binder has hydrophobic nature. PBI binder is easily covered on the surface of the Pt catalyst particles because of its hydrophilic nature. Therefore, the low gas permeability in PBI polymer film formed on the Pt catalyst sites could lead to mass transport limitation in catalyst layer. Otherwise, PVDF binder prevents the formation of the agglomerates of the catalyst particles in the catalyst layer, and provides more Pt surface in the catalyst layer. In addition, the PA in the PBI membrane is transferred to catalyst layer with hot press process. PBI binder allows PA transferring while, PVDF binder prevents PA transferring to catalyst layer. Because of all these reasons, PVDF binder provides higher performance for the fuel cell than that for the PBI binder, as shown in Figure 5.3. The power densities at 0.6 V for PBI and PVDF binders were found as 0.13 W/cm^2 and 0.25 W/cm^2, respectively.

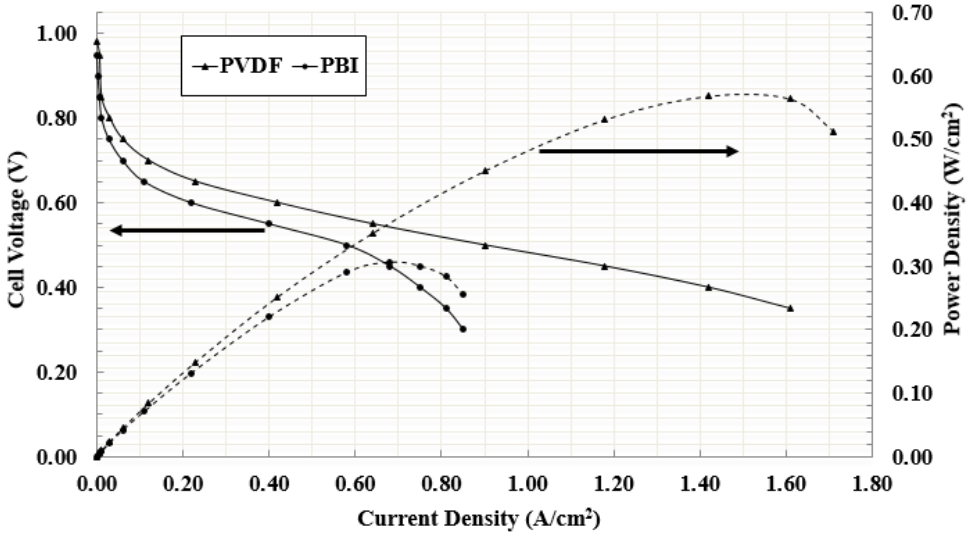

Figure 5.3 The polarization curves of experimental study for different binders

5.3 One-dimensional and Semi-Empirical Modeling of HT-PEMFC

The calibration of parameters, the effect of some parameters (operating cell temperature and the amount of CO) in the HT-PEMFC model based on PBI binder, the effect of some parameters (operating cell temperature, Pt loadings, and phosphoric acid percentage) in the HT-PEMFC model based on PVDF binder, and the effect of different binders, are presented in this section.

5.3.1 Calibration of parameters

In this section, three modeling parameters (the thin electrolyte film thicknesses for anode and cathode and the contact resistance) were calibrated using experimental data, which include i-V values at different Pt loadings (0.6 mg/cm^2, 1 mg/ cm^2, and 1.5 mg/cm^2), cell temperatures (1601°C, 180°C, and 200°C), and binder type (PBI and PVDF). To calibrate these parameters, the total summation of the square of the difference between the cell voltages found using the experimental and modeling methods (Eq. (5.1)) is minimized using Genetic Algorithm. In this equation, n is the total number of data points taken from the polarization curve. Upper and lower bounds of these calibrated parameters were decided after carrying out a comprehensive literature survey (Bouchet and Siebert, 1999; Dhar et al., 1986; Liang et al., 2015;

Mench,2008). The calibrated parameters and the bounds for both PBI and PVDF binders are shown in Table 5.1.

$$Error = \sum_{j=1}^{n} \left(E_{cell} - E_{exp}\right)^2 \quad (5.1)$$

Table 5.1 The calibrated parameters for both PBI and PVDF binder

Parameters	**Minimum value**	**Maximum value**
Anode thin electrolyte film thickness (δ_a)	$2.5 \cdot 10^{-7}$ cm	$8 \cdot 10^{-6}$ cm
Cathode thin electrolyte film thickness (δ_c)	$1.48 \cdot 10^{-7}$ cm	$8 \cdot 10^{-6}$ cm
Contact Resistance ($R_{contact}$)	0.00001 Ω·cm^2	0.004 Ω·cm^2

The values of the calibration parameters for each case were found. For example, the values of δ_a, δ_c and $R_{contact}$ at the Pt loading of 1.5 mg/cm^2 and cell temperature of 160°C were found as $4.70 \cdot 10^{-6}$ cm, $4.60 \cdot 10^{-6}$ cm, and 0.004 Ω·cm^2 for PBI binder, respectively, and $2.83 \cdot 10^{-6}$ cm, $3.29 \cdot 10^{-6}$ cm, and 0.004 Ω·cm^2 for PVDF binder, respectively. Using these values and the input parameters given in Tables 4.1 and 4.2, the polarization curves of the model were obtained for both PBI and PVDF binders, as shown in Figure 5.4. As can be also seen in this figure, the model-based polarization curves match well with the experimental data for both binders.

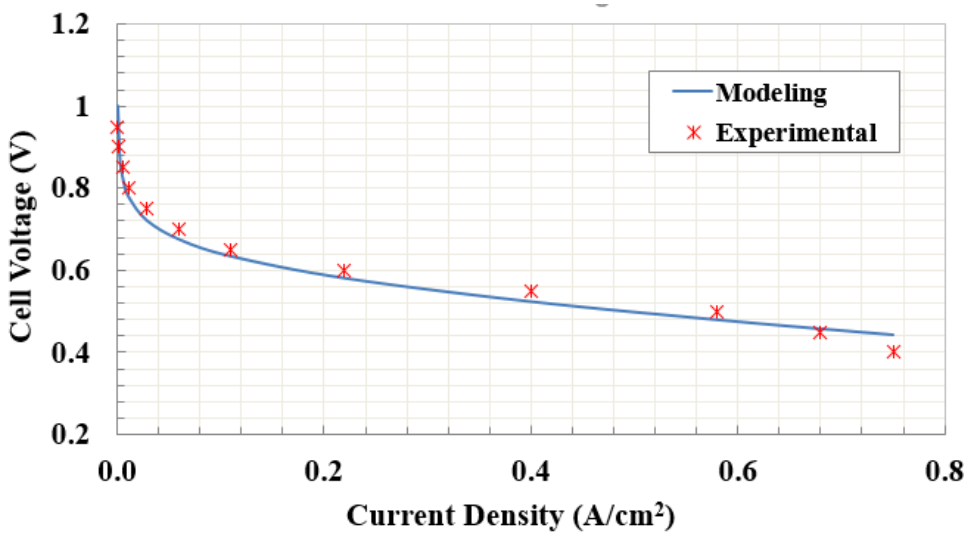

(a)

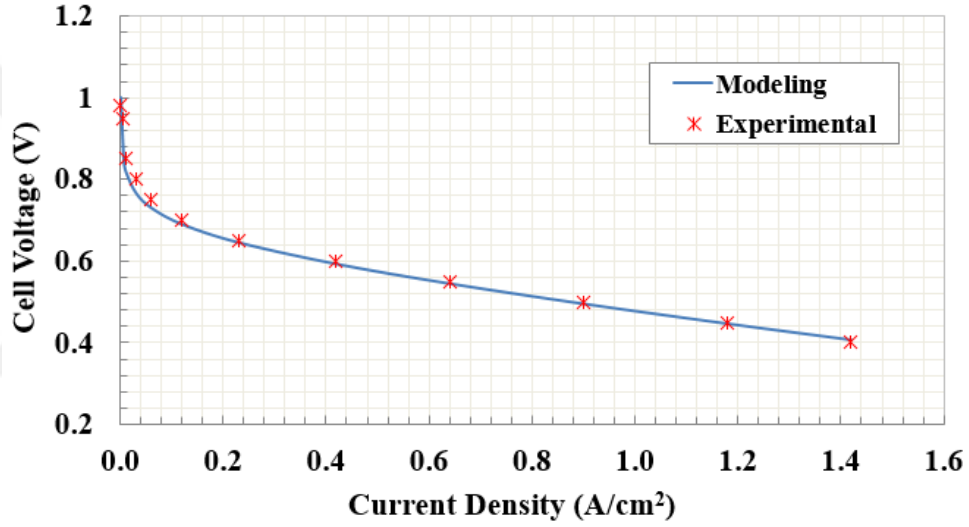

(b)

Figure 5.4 Polarization curves based on the modeling and experimental results for HT-PEMFC having a) PBI binder and b) PVDF binder

5.3.2 The HT-PEMFC model based on PBI binder

5.3.2.1 Effect of operating cell temperature

Figure 5.5 shows the polarization curves of HT-PEMFC operating at different cell temperatures (160°C, 180°C, and 200°C). According to Figure 5.5, it was found that when the cell temperature increases, the performance of the fuel cell increases. The reason of the performance increment of the fuel cell is that when the cell temperature increases, the rate of reaction kinetics and the proton conductivity of the PBI membrane increase. Using Eq. (4.37), the proton conductivities were calculated as

0.191 S/cm at 160°C and 0.316 S/cm at 200°C. The power densities calculated at 0.5 V at 160°C, 180°C, and 200°C are 0.25 W/cm^2, 0.28 W/cm^2, and 0.31 W/cm^2, respectively. The increase of power density at this cell voltage is found to be 24% when the cell temperature is increased from 160°C to 200°C.

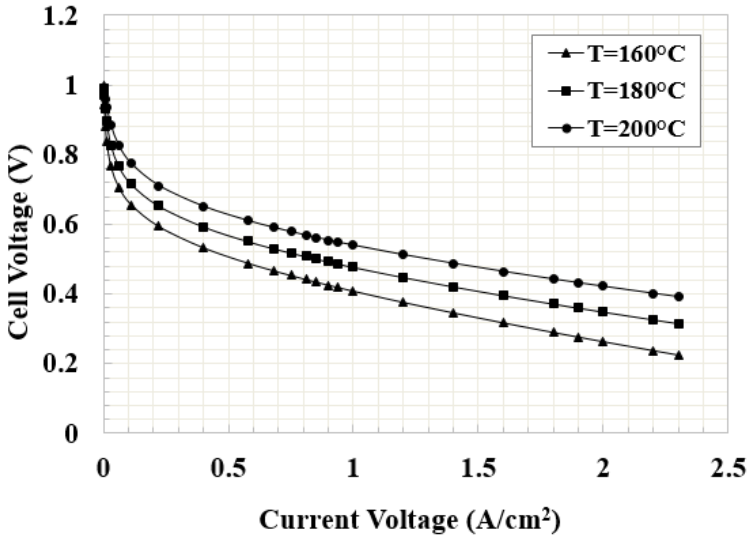

Figure 5.5 The polarization curves of HT-PEMFC model at different operating cell temperatures

5.3.2.2 Effect of the Amount of CO

Figure 5.6 shows the change of cell voltage with respect to current density for various gas mixtures. Four different cases are taken in which the H_2, CO, and CO_2 mole fractions are altered. These cases are as follows:

- 100 % H_2 (Pure hydrogen)
- 75% H_2 + 24% CO_2 + 1% CO
- 60% H_2 + 39% CO_2 + 1% CO
- 60% H_2 + 35% CO_2 + 5% CO

The polarization curves obtained for each of these cases are given in Figure 5.6. As expected, under the same current density and operating temperature (160°C), pure H_2 gives the best performance among the other reformate gases. When the CO mole fraction is taken as constant (1%), decreasing the mole fraction of H_2 decreases the

performance of fuel cell. It can be concluded that the H_2 percentage in the reformate gas is the most important parameter affecting the performance of fuel cell. On the other hand, when the H_2 mole fraction is taken as constant (60%), increasing the mole fraction of CO decreases the performance of fuel cell. Thus, the increasing CO percentage affects the performance negatively. Consequently, when the mole fraction of H_2 decreases from 75% to 60%, the cell voltages of the fuel cell decrease by 2.77% and 4.40%, respectively, compared to pure H_2 for a HT-PEMFC operating at 0.75 A/cm^2. When the mole fraction of CO increases from 1% to 5%, the cell voltages of the fuel cell decrease by 4.40% and 6.18%, respectively, compared to pure H_2 for a HT-PEMFC operating at 0.75 A/cm^2.

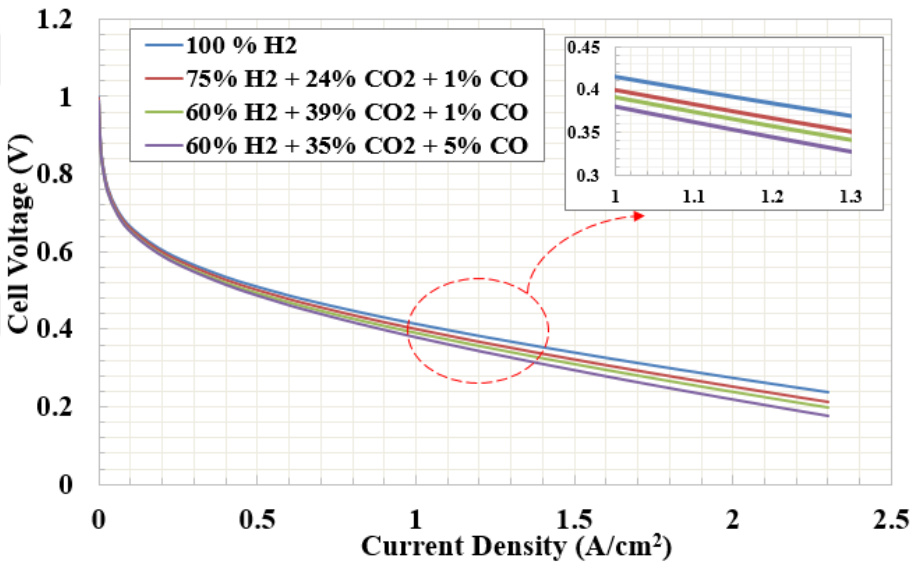

Figure 5.6 The polarization curves in the anode for various gas mixtures at 160°C

The polarization curves of fuel cell operating at 160°C with pure H_2 and H_2 containing CO are shown in Figure 5.7. Similar to Figure 5.6, when the CO percentage increases, the performance of fuel cell decreases and pure H_2 gives the best performance compared to others.

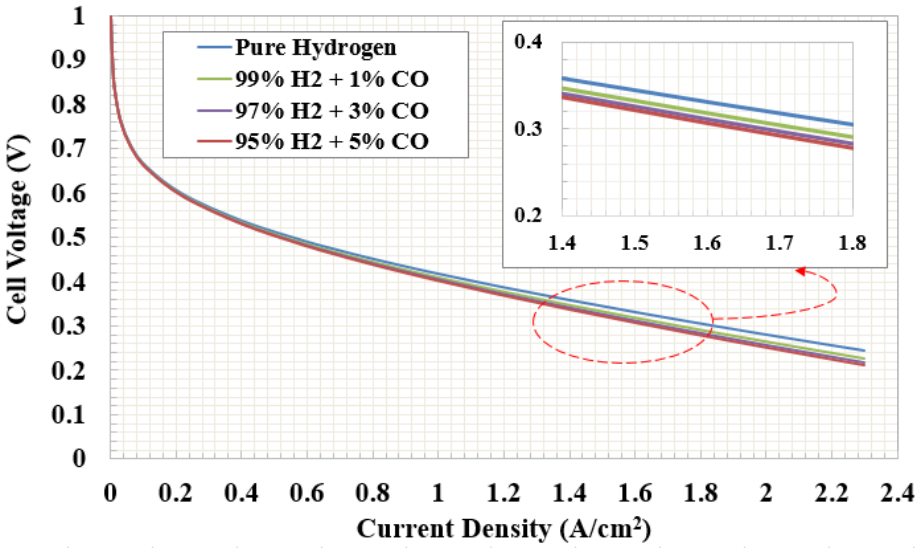

Figure 5.7 The polarization curves according to CO percentage in the reformate gas at 160°C

Figure 5.8 shows the effects of both temperature and CO percentage on the performance of fuel cell. It is found that when the CO percentage is changed from 1% CO to 5% CO, the cell voltage decreases by 1.07% for 160°C; whereas the cell voltage decreases by 0.45% for 200°C. The difference between the polarization curves at 160°C is more than the difference between the polarization curves at 200°C. It can be concluded that when the temperature increases, CO poisoning effect decreases.

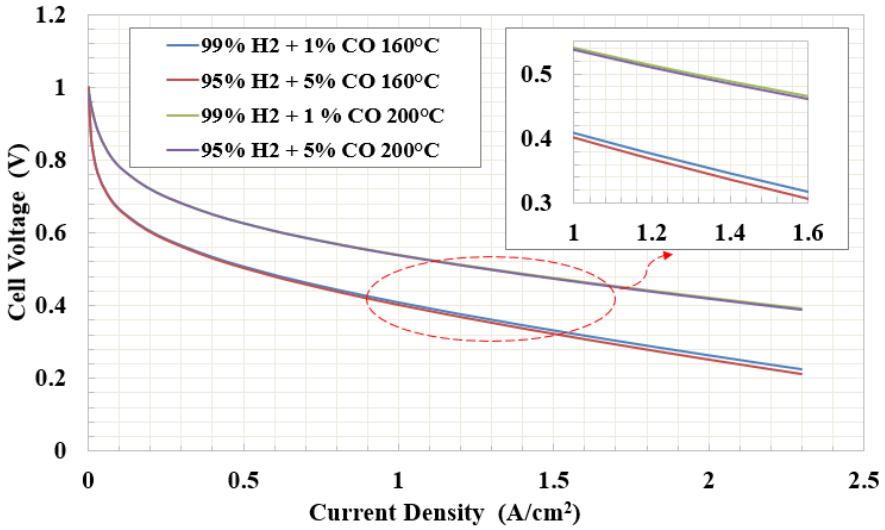

Figure 5.8 The polarization curves according to CO percentage and temperature

From Figures 5.6, 5.7 and 5.8, it can be seen that the amount of CO effect is not significant at low current density conditions since the Pt sites that do not cover CO are enough to support H_2 oxidation reaction. As current density increases, the H_2 oxidation reaction is restricted by Pt sites that include CO adsorption and the performance of fuel cell decreases.

5.3.3 The HT-PEMFC model based on PVDF binder

5.3.3.1 Effect of operating cell temperature

Figure 5.9 shows the polarization curves of HT-PEMFC operating at different cell temperatures (160°C, 180°C, and 200°C). According to Figure 5.9, it was found that when the cell temperature increases, the performance of the fuel cell increases. The reason of the performance increment of the fuel cell is that when the cell temperature increases, the rate of reaction kinetics and the proton conductivity of the PBI membrane increase. Using Eq. (4.37) which was found by experimental data, the proton conductivities were calculated as 0.191 S/cm at 160°C, 0.248 S/cm at 180°C, and 0.316 S/cm at 200°C. The power densities calculated at 160°C, 180°C, and 200°C are 0.45 W/cm^2, 0.48 W/cm^2, and 0.52 W/cm^2, respectively, for the cell voltage of 0.5 V. The increase of power density at this cell voltage is found to be 17.55% when the cell temperature is increased from 160°C to 200°C. However, it should be noted that when the cell temperature increases, degradation rate increases, which affects the long-term stability of the HT-PEMFCs negatively. In addition, start-up time to bring the cell to the desired cell temperature increases.

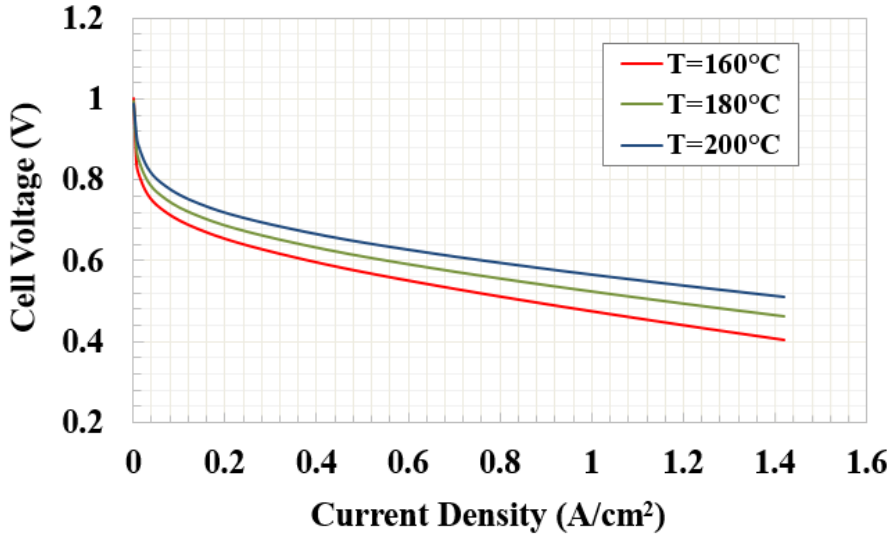

Figure 5.9 The polarization curves of HT-PEMFC operating at different cell temperatures

5.3.3.2 Effect of Pt loading

Figure 5.10 shows the polarization curves of HT-PEMFC having different platinum loadings (0.6 mg/cm^2, 1 mg/cm^2, and 1.5 mg/cm^2). It can be seen from this figure that when the Pt loading increases, the performance of the fuel cell increases, which can be explained as follows. Thin film thickness is affected by the total volume of binder, Pt, and C in the catalyst layer. The relationship between this volume, the thin electrolyte film thickness, and other related electrochemical and geometrical parameters is shown in the study of Sousa et al. (2010) as follows.

$$\delta = \left\{ \left(\frac{\frac{L_{PA}}{\rho_{PA}} \cdot A - \frac{\varepsilon_{agg} \cdot V_{solids}}{1-\varepsilon_{agg}}}{V_{solids}} + V_{agg} \right) \cdot \frac{3}{4\pi} \right\}^{1/3} - r_{agg} \qquad (5.2)$$

where L_{PA} and ρ_{PA} are the mass of PA per area and the density of PA, A is catalyst layer area, V_{agg} and r_{agg} are the volume and radius of agglomerate, and V_{solids} is the total volume of solids (Pt, C, and binder (PVDF)) in the catalyst layer. As can be seen from this equation, when the amounts of binder, Pt, and C increase, the thin electrolyte film thickness decreases. The thin electrolyte film thicknesses of the anode for a HT-

PEMFC at 160°C were calculated as $5.59 \cdot 10^{-6}$ cm (for 0.6 mg/cm^2 Pt loading), $3.78 \cdot 10^{-6}$ cm (for 1 mg/cm^2 Pt loading), and $2.83 \cdot 10^{-6}$ cm (for 1.5 mg/cm^2 Pt loading); whereas those of the cathode were calculated as $5.47 \cdot 10^{-6}$ cm (for 0.6 mg/cm^2 Pt loading), $3.84 \cdot 10^{-6}$ cm (for 1 mg/cm^2 Pt loading), and $3.29 \cdot 10^{-6}$ cm (for 1.5 mg/cm^2 Pt loading). The decreases of thin film thicknesses for anode and cathode are found to be 49% and 39% when the Pt loading is increased from 0.6 mg/cm^2 to 1.5 mg/cm^2, respectively. Therefore, as can be seen from Eqs. (4.19) and (4.20), when the thin electrolyte film thickness decreases, the difference between dissolved concentration and the concentration on the Pt surface for H_2 and O_2 decreases, and the performance of the fuel cell increases. The power densities at 0.5 V were calculated as 0.30 W/cm^2 (for 0.6 mg/cm^2 Pt loading), 0.39 W/cm^2 (for 1 mg/cm^2 Pt loading), and 0.44 W/cm^2 (for 1.5 mg/cm^2 Pt loading). The increase of power density at this cell voltage is found to be 46% when the Pt loading is increased from 0.6 mg/cm^2 to 1.5 mg/cm^2.

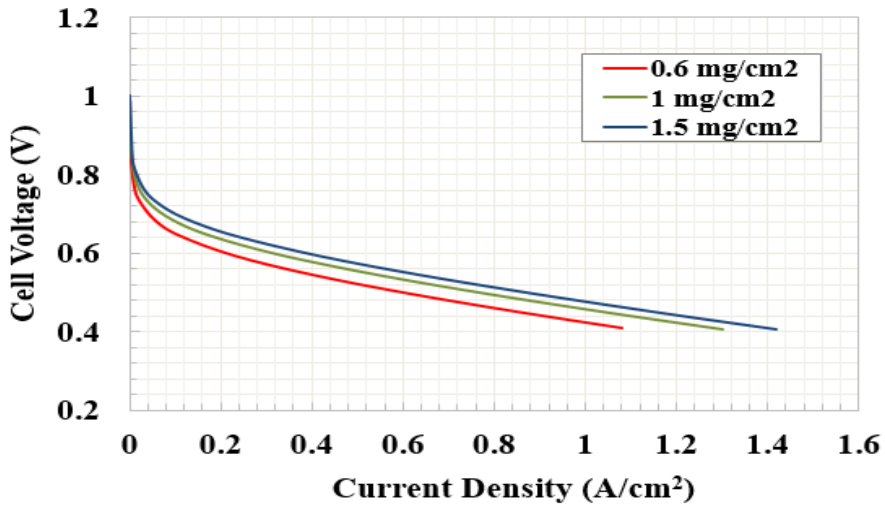

Figure 5.10 The polarization curves of HT-PEMFC having different platinum loadings

5.3.3.3 Effect of Phosphoric acid percentage

The effect of PA percentage on the performance of the HT-PEMFC was studied and the results are presented in this section. Figure 5.11 shows the polarization curves of HT-PEMFC having different PA percentage (70%, 75%, 80%, 85%, and 90% of PA percentage). According to Figure 5.11, the cell voltages at 0.42 A/cm^2 for 70%, 75%, 80%, 85%, and 90% of PA percentage are found as 0.530 V, 0.565 V, 0.586 V,

0.591 V, and 0.580 V, respectively. The percentage of PA affects the Henry's constant and diffusion coefficient of O_2 and H_2, as shown in Eqs. (4.23)-(4.26). When the Henry's constant decreases, the dissolved concentration increases, and therefore, the concentration of H_2 and O_2 on the platinum surface increases. When the diffusion coefficients of H_2 and O_2 increases, the concentration on the platinum surface increases. Consequently, the performance of the fuel cell increases, as shown in Eq. (4.29). When the percentage of PA changes from 70% to 85%, the Henry's constant decreases and the diffusion coefficient increases, and therefore, the performance of the fuel cell increases. However, when the percentage of PA is more than 85%, the Henry's constant increases and the diffusion coefficient decreases, and therefore, the performance of the fuel cell decreases. In addition to these, if the PA percentage is higher than a certain value, it covers the surface of catalyst layer and diffuses into the pores of this layer, and blocks the voids. Due to this reason, the reaction gases would not easily reach to the catalyst layer where the reactions occur, which in turn would decrease the performance of the fuel cell (Ergun et al., 2012). It should be also noted that increasing PA percentage affects negatively the mechanical stability of PBI membrane (Bhadra et al., 2010).

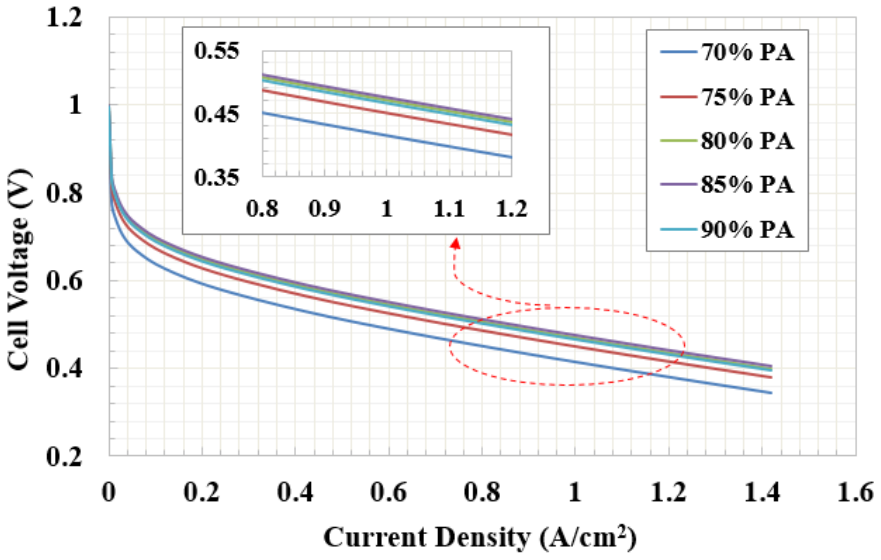

Figure 5.11 The polarization curves of HT-PEMFC having different PA percentages

5.3.4 The effect of different binders

The binder material used in the preparation of the catalyst ink is a critical component as it regulates the hydrophobicity and hydrophilicity of the catalyst layer and also forms the triple phase boundary for electrolyte, catalyst, and reactant gases (Kim et al., 2015). When the amount of binder in the catalyst ink is too little, the proton conductivity decreases and the transport losses increase. However, when the amount of binder in the catalyst ink is too much, the catalyst layer becomes moist and the diffusion of the reactant gases to the reaction sites slow down (Zamel, 2016). Typical binders are PBI, PVDF, PTFE, and PBI-PVDF for HT-PEMFCs.

In this study, the effects of PBI and PVDF binders on the fuel cell performance were examined. It was found that the PVDF binder provides higher performance for the fuel cell than that for the PBI binder, as shown in Figure 5.12. This finding can be explained as follows. When the PBI binder was used, the electrolyte thin film thicknesses of anode and cathode were found as $4.70 \cdot 10^{-6}$ cm and $4.60 \cdot 10^{-6}$ cm, respectively. On the contrary, when the PVDF binder was used, the electrolyte thin film thicknesses of anode and cathode were found as $2.83 \cdot 10^{-6}$ cm and $3.29 \cdot 10^{-6}$ cm, respectively. As mentioned in Section 5.3.3.2, when the thin electrolyte film thickness decreases, the performance of the fuel cell increases. When the PVDF binder is used in catalyst ink, the thin electrolyte film thicknesses for anode and cathode were found less than those of the PBI binder. Moreover, the cell voltages at 0.42 A/cm^2 for PBI and PVDF binders were found as 0.525 V and 0.591 V, respectively. The increase of cell voltage at this current density was found to be 12.57% when the binder type changed from PBI to PVDF. Therefore, the MEA with the PVDF binder showed better performance than that with the PBI binder. In addition to these, due to the hydrophilic nature of PBI binder, this binder is easily covered on the surface of the Pt catalyst particles, which could lead to mass transport limitation in catalyst layer due to the low gas permeability in PBI polymer film formed on the Pt catalyst sites. Hydrophobic nature of the PVDF binder prevents the formation of the agglomerates of the catalyst particles in the binder, and enables more Pt surface in the catalyst layer (Su et al., 2013b). In addition, the transport of product water in the electrode could be balanced by using highly

hydrophobic PVDF binder. The elimination of liquid water can also increase the exposed surface area of the Pt catalysts and improve the ability of the H_2 and reactants to diffuse into the reaction layers (Su et al., 2013b).

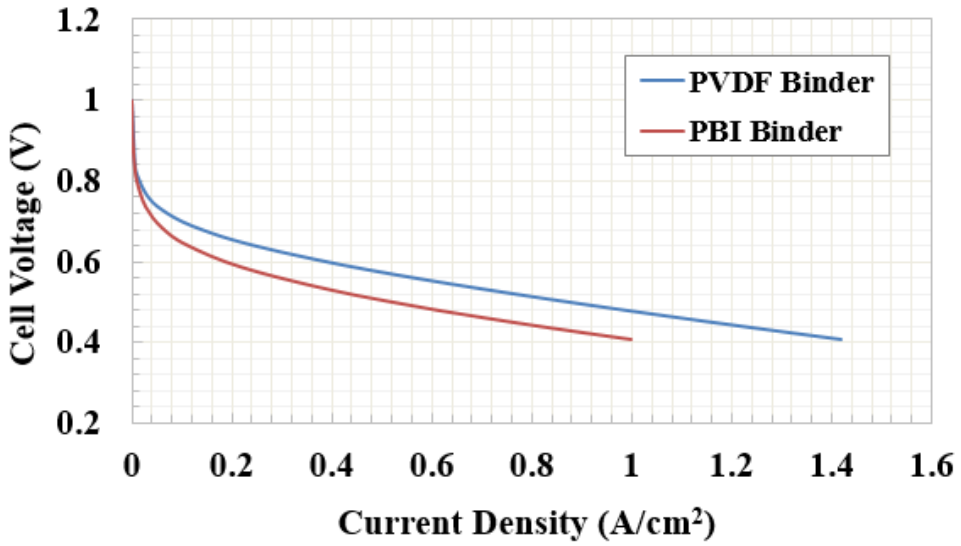

Figure 5.12 The polarization curves of HT-PEMFC having different binders

5.4 The mathematical model for a HT-PEMFC stack based a simple cogeneration system

5.4.1 The effect of anode stoichiometry ratio

Stoichiometric ratio is defined as the ratio between the actual reactant flow rate at the inlet of fuel cell and the consumption flow rate in the electrochemical reaction (theoretical flow rate). The stoichiometric ratio for anode side is preferred as 1 or slightly higher. If the pure H_2 is supplied to fuel cell, the surplus of H_2 can be used again in the electrochemical reaction and fed back to fuel cell. This case is called as deal-end mode (Barbir, 2005). However, if H_2 is not pure (e.g. reformate gas), the surplus of H_2 leaves from fuel cell and does not react. When the molar flow rate is high, the efficiency of fuel cell will be low because of waste H_2 whereas, when the molar flow rate is low, the performance of the fuel cell can decrease. The flow rate of the reactant fed to the fuel cell must be slightly higher due to the losses (e.g. internal

currents and crossover permeation) in the fuel cell than the flow rate consumed in the electrochemical reaction to produce the electric current (Barbir, 2005).

Figure 5.13 shows the effect of anode stoichiometry ratio on the electrical efficiency. Anode stoichiometry ratio mainly affects the molar flow rate of H_2 as shown in Table 5.2. According to Figure 5.13, it is found that when the anode stoichiometry ratio increases, the molar flow rate of H_2 increases, and the electrical efficiency for the system decreases. The electrical efficiencies at 0.42 A/cm^2 for 1.2, 2.0, and 2.5 stoichiometries were calculated as 40%, 25%, and 18%, respectively. Fuel utilization efficiencies for 1.2, 2.0, and 2.5 stoichiometries were calculated 85%, 52%, and 39%, respectively. The decrease of fuel utilization efficiency at this current density is found to be 54% when the anode stoichiometry ratio increases from 1.2 to 2.5.

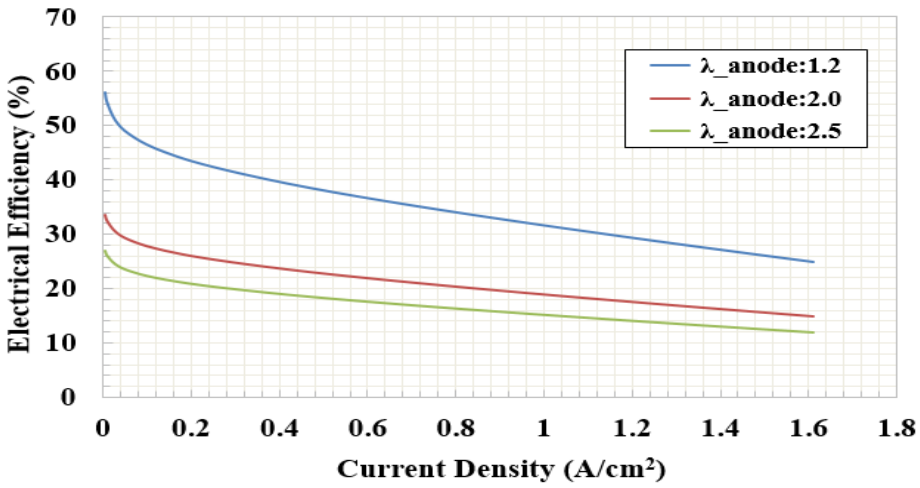

Figure 5.13 The effect of anode stoichiometry ratio on the electrical efficiency

5.4.2 The average temperature of hot water for each month

In houses, the ideal temperature for taking shower is between 33°C and 38°C. The temperatures of pre-wash, wash, and rinsing in a dishwasher are 30-35°C, 50-60°C, and 80-90°C, respectively. The average temperature of water in a washing machine is 20-90°C for different program levels. Figure 5.14 shows that the temperature increases at 0.42 A/cm^2 and 1.61 A/cm^2 were found as 2.62 °C and 13.30 °C, respectively. In addition, the temperature increases at 1.61 A/cm^2 for 13 and 26 cells were found as

13.30°C and 26.60°C, respectively. The results show that this cogeneration system is suitable for the house needs discussed above.

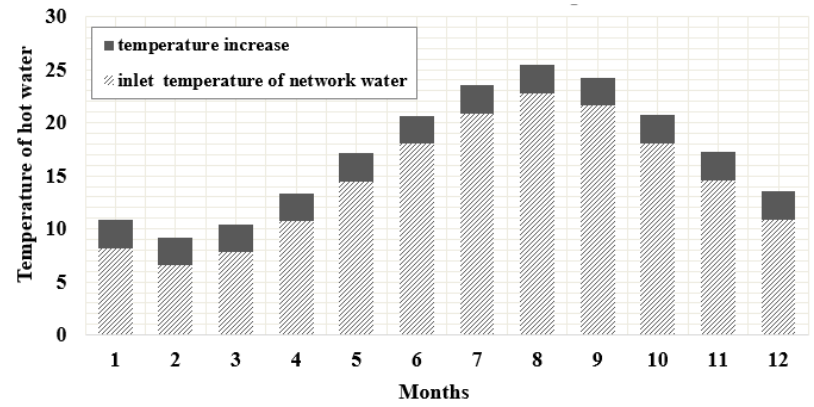

(a)

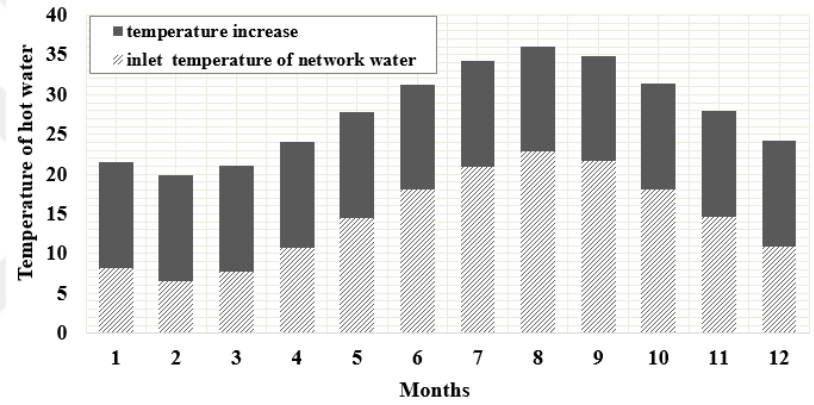

(b)

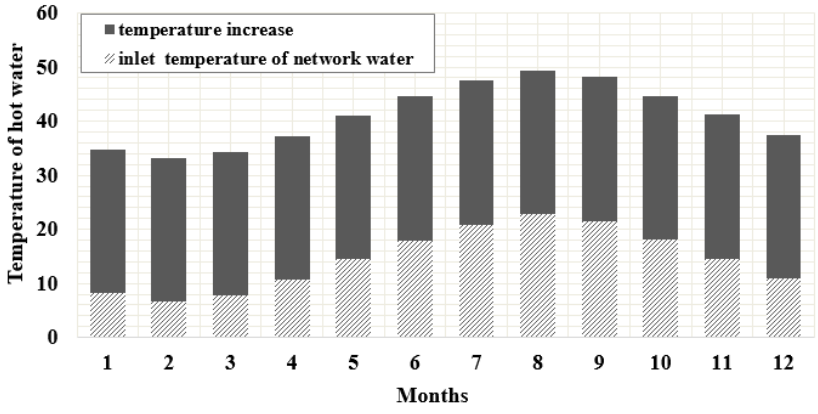

(c)

Figure 5.14 The average temperature of hot water for each month at (a) 0.42 A/cm^2 for 13 cells, (b) 1.61 A/cm^2 for 13 cells, and (c) 1.61 A/cm^2 for 26 cells

5.5 The thermodynamic model for a cogeneration system (including HT-PEMFC, SMR, WGS, and burner) that converts natural gas into electricity and heat

The HT-PEMFC based cogeneration system shown in Figure 4.5 is thermodynamically modeled using EES software. In this section, the results and discussions of both energy and exergy analyses are given in detail.

5.5.1 Energy analysis of HT-PEMFC based cogeneration system

In this section, the effects of steam-to-carbon ratio (SCR), fuel cell operating temperature, and anode stoichiometric ratio on the system performance (electrical efficiency and cogeneration efficiency) are examined parametrically. In Table 5.2, the range of the selected parameters and the values used in the model are given. Table 5.3 gives the temperatures and molar flow rates for each point in the cogeneration system.

Table 5.2 Value and range of selected parameters

Parameter	**Value**	**Range**
Steam-to-carbon ratio, SCR	2	1-2
Fuel cell operating temperature, T_{cell}	160 °C	120-200 °C
Anode stoichiometric ratio, λ_{H_2}	1.2	1.2-2

Table 5.3 Molar flow rates and temperatures for each state in the cogeneration system

State	Molar flow rate, $\dot{n}$ (mol/s)	Temperature, T (K)
1	0.04106	298.2
2	0.04106	298.2
3	0.01145	298.2
4	0.01145	453.9
5	0.005723	298.2
6	0.005723	298.2
7	0.01717	398.2
8	0.02416	723.2
9	0.02416	523.2
10	0.02561	523.1
11	0.02561	433.2
12	0.01152	433.2
13	0.02142	298.2
14	0.0004751	298.2
15	0.0005142	433.2
16	0.0005142	280
17	0.02095	298.2
18	0.02961	298.2
19	0.02961	302.8
20	0.02961	303.9
21	0.02961	411.2
22	0.02961	442.1
23	0.02961	513
24	0.3061	368.2
25	0.3061	397
26	0.3061	368.2
27	0.3061	368.2
28	0.03107	1966
29	0.03107	680.6
30	0.03107	625.7
31	0.03107	400

5.5.1.1 The effect of steam-to-carbon ratio on the performance of the cogeneration system

The necessary H_2 molar flow rate for the HT-PEMFC to provide sufficient power in the cogeneration system was calculated using the Faraday Law. The molar flow rates of water and CH_4 entering the SMR based on the H_2 molar flow rate in the reformate gas (CH_4, CO, H_2, CO_2, and H_2O) at the inlet of the HT-PEMFC are calculated by the given SCR value. The SCR value is defined by the equation shown in Eq. (5.2).

$$SCR = \frac{\dot{n}_{H_2O,input}}{\dot{n}_{CH_4,input}} \tag{5.2}$$

Table 5.4 shows parametrically the effects of steam-to-carbon ratio (SCR) on the molar flow rates of H_2O and CH_4, the total waste heat recovered from the heat exchangers, and the electrical and cogeneration efficiencies. Figure 5.15 shows the change of the electrical efficiency and cogeneration efficiency with the SCR. When the SCR ratio is increased from 1 to 2, the electrical efficiency increases from 13.15% to 26.28%, while the cogeneration efficiency decreases from 83.04% to 70.34%. Because, when the SCR increases, the molar flow rate of the CH_4 entering the system decreases by 48.62%, and the molar flow rate of the water entering the SMR reactor increases by 2.69%. The electrical efficiency of the system (Eq. (4.69)) has increased with increasing CH_4 molar flow rate and increasing net electric power (2.62%). When the SCR increases, the total waste heat recovered from the heat exchangers decreases by 67.69%. Despite the increased molar flow rate of CH_4, the decrease in the total waste heat recovered from the heat exchangers shows a 15.30% reduction in cogeneration efficiency (Eq. (4.70)).

Table 5.4 Effect of steam-to-carbon ratio on the system performance

SCR	$\dot{n}_{H_2O,input}$ **(mol/s)**	$\dot{n}_{CH_4,input}$ **(mol/s)**	$\dot{W}_{net,electrical}$ **(W)**	$\dot{Q}_{HEX,cogen}$ **(W)**	$\eta_{electrical}$	$\eta_{cogeneration}$
1	0.04012	0.01114	1176	6250	0.1315	0.8304
1.111	0.04021	0.01005	1182	5400	0.1465	0.8159
1.222	0.0403	0.009159	1187	4705	0.1615	0.8016
1.333	0.04039	0.008415	1192	4125	0.1765	0.7873
1.444	0.04049	0.007786	1195	3635	0.1913	0.7731
1.556	0.04059	0.007249	1198	3217	0.206	0.7589
1.667	0.04071	0.006785	1201	2855	0.2206	0.7449
1.778	0.04085	0.006382	1203	2541	0.2349	0.7309
1.889	0.04101	0.006031	1205	2265	0.249	0.7171
2	0.0412	0.005723	1207	2023	0.2628	0.7034

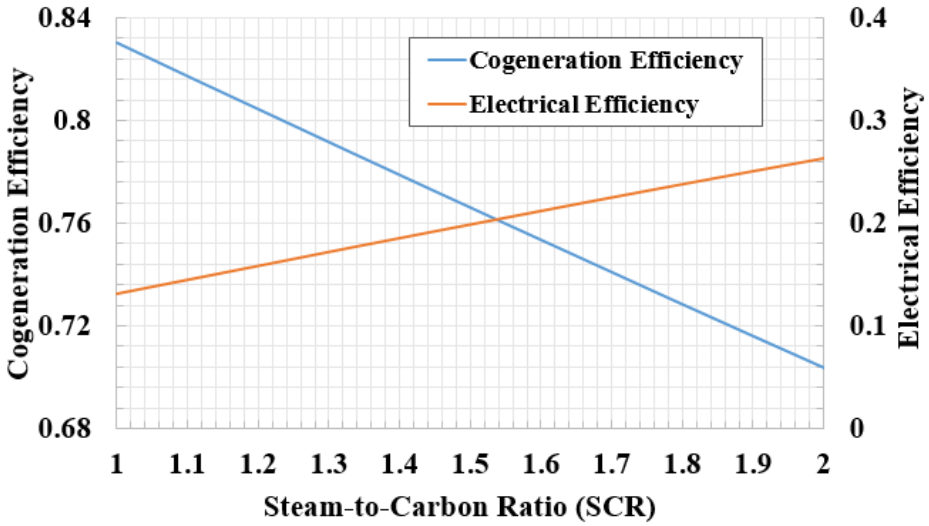

Figure 5.15 The change of electrical and cogeneration efficiencies with SCR

5.5.1.2 The effect of fuel cell operating temperature on the performance of the cogeneration system

In Section 5.3.3.1, the effect of the fuel cell operating temperature on the performance of the fuel cell was investigated. When the fuel cell operating temperature increased, the performance of the fuel cell was found to increase and this result is given. In this section, the effects of the fuel cell operating temperature on the performance (cogeneration and electrical efficiencies) of the system based on the change interval given in Table 5.3 were examined parametrically. Table 5.5 gives the effects of the fuel cell operating temperature on the total waste heat recovered from the heat exchangers and on the electrical and cogeneration efficiencies of the system.

According to Table 5.5, when the fuel cell operating temperature increases, the amount of waste heat recovered from HEX-1 does not change. The amounts of waste heat recovered from HEX-2 and HEX-4 decrease; whereas those from HEX-3 and HEX-5 increase. Thus, as the temperature increases, the amount of waste heat recovered from the total heat exchangers decreases by 17.16%, while the net electrical power of the system increases by 37.21%. Figure 5.16 shows the decrease in the efficiency of cogeneration and the increase in electrical efficiency. When the fuel cell operating temperature increases from 120 ° C to 200 ° C, the system's electrical

efficiency and cogeneration efficiency increase by 37.41% and decrease by 0.36%, respectively.

Table 5.5 Effect of operating cell temperature on system performance

T_{cell} (°C)	$\dot{Q}_{HEX,1}$ (W)	$\dot{Q}_{HEX,2}$ (W)	$\dot{Q}_{HEX,3}$ (W)	$\dot{Q}_{HEX,4}$ (W)	$\dot{Q}_{HEX,5}$ (W)	$\dot{Q}_{HEX,cogen}$ (W)	$\dot{W}_{net,elec}$ (W)	η_{elec}	η_{cogen}
120	158.1	98.88	1.742	1761	223.2	2237	998.4	0.2162	0.7047
128.9	158.1	92.2	1.879	1704	226.8	2177	1057	0.229	0.7044
137.8	158.1	85.51	2.016	1656	230.3	2126	1107	0.2398	0.7041
146.7	158.1	78.81	2.153	1613	233.9	2080	1151	0.2495	0.7038
155.6	158.1	72.1	2.291	1574	237.5	2037	1193	0.2585	0.7036
164.4	158.1	65.38	2.429	1537	241.2	1997	1231	0.267	0.7033
173.3	158.1	58.64	2.567	1502	244.8	1959	1268	0.275	0.703
182.2	158.1	51.89	2.705	1468	248.5	1923	1303	0.2826	0.7027
191.1	158.1	45.13	2.843	1436	252.1	1888	1337	0.29	0.7024
200	158.1	38.36	2.981	1405	255.8	1853	1370	0.2971	0.7021

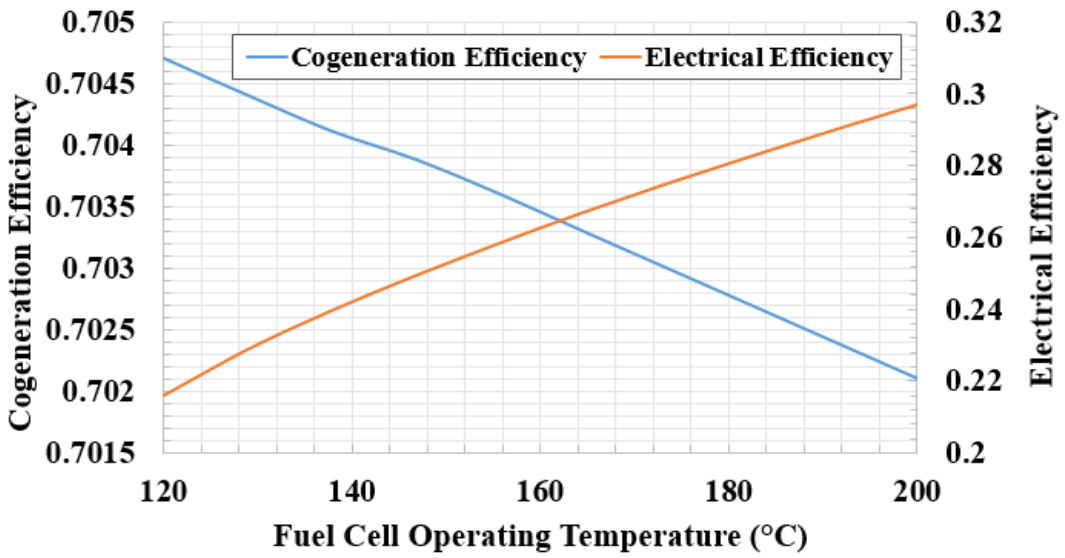

Figure 5.16 The change of electrical and cogeneration efficiencies with fuel cell operating temperature

5.5.1.3 The effect of anode stoichiometric ratio on the performance of the cogeneration system

CH_4 and H_2O sent from the outside of the system pass through the fuel processing system and form a hydrogen rich-reformate gas (CH_4, CO, CO_2, H_2, and H_2O). This reformate gas is supplied from the anode side to the fuel cell in this cogeneration system. As mentioned in Section 5.4.1, if fuel cell is not supplied with pure H_2, excess H_2 not involved in the electrochemical reaction cannot be reused. Therefore, anode

stoichiometric ratio is not chosen as 1. The greater the stoichiometric ratio of the anode is, the higher the molar flow rate is and the lower the performance due to the waste H_2 is. For this reason, considering the losses, the anode stoichiometric ratio was chosen as 1.2 in this system. Table 5.6 shows the effect of anode stoichiometric ratio on the electrical efficiency and cogeneration efficiency.

According to Table 5.6, when the anode stoichiometric ratio increases, the molar flow rate of H_2 increases. If the molar flow rate of H_2 increases at a constant steam-to-carbon ratio, the molar flow rates of CH_4 and H_2O sent to the system also increase. Therefore, the electrical efficiency and cogeneration efficiency decrease. Figure 5.17 shows the decreases of cogeneration efficiency and electrical efficiency. When the anode stoichiometric ratio increases from 1 to 2, the electrical efficiency and cogeneration efficiency decrease by 42.04% and 33.15%, respectively.

Table 5.6 Effect of anode stoichiometric ratio on system performance

λ_{H_2}	$\eta_{electrical}$	$\eta_{cogeneration}$	$\dot{Q}_{HEX,cogen}$ (W)	$\dot{W}_{net,electrical}$ (W)
1.2	0.2628	0.7034	2023	1207
1.3	0.2415	0.658	2076	1204
1.4	0.2233	0.6192	2129	1200
1.5	0.2075	0.5858	2183	1197
1.6	0.1937	0.5567	2237	1194
1.7	0.1815	0.5311	2293	1191
1.8	0.1707	0.5084	2349	1187
1.9	0.161	0.4883	2406	1184
2	0.1523	0.4702	2464	1181

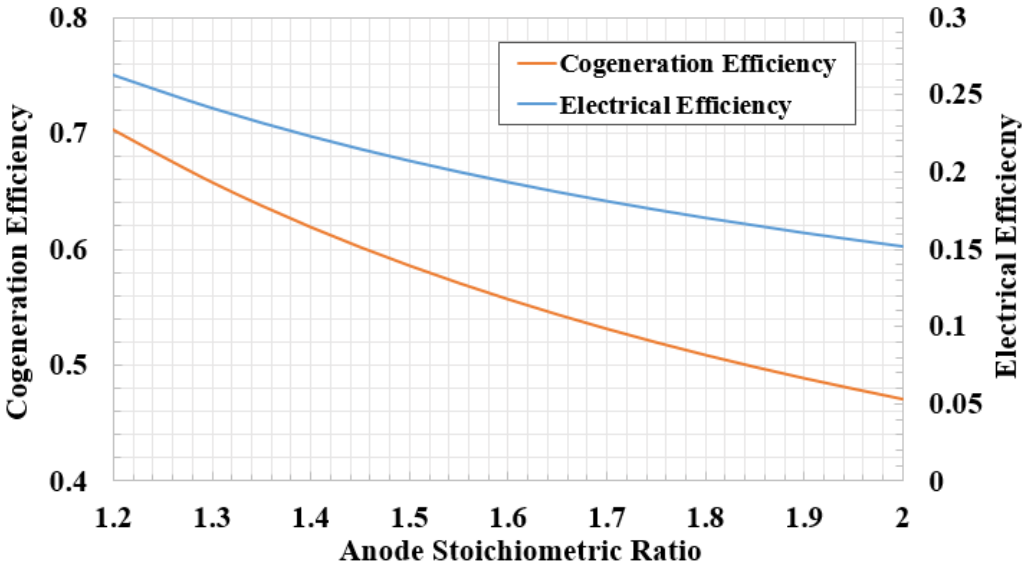

Figure 5.17 The change of electrical and cogeneration efficiencies with anode stoichiometric ratio

5.5.2 Exergy analysis of HT-PEMFC based cogeneration system

In this section, the effects of steam-carbon ratio (SCR), fuel cell operating temperature, and anode stoichiometric ratio on the exergetic efficiency of the cogeneration system and the exergy destructions of components are examined parametrically. In Table 5.8, the values of exergy destruction of each component are given. Table 5.9 gives the values of physical exergy, chemical exergy, and total exergy for each point in the cogeneration system.

Table 5.8 The values of exergy destruction for each component in the system

Component	**Exergy destruction, $\dot{E}x_D$, kW**	**Component**	**Exergy destruction, $\dot{E}x_D$, kW**
Water Pump	71.29	HT-PEMFC Stack	1640
Compressor	0.3525	HEX-1	73.55
Mixer	3194	HEX-2	2.573
SMR	628.4	HEX-3	0.3997
WGS	115	HEX-4	334.4
Catalytic Burner	625.9	HEX-5	82.88

The distribution of ratio between the exergy destruction rate of a component and the exergy rate of the fuel supplied to cogeneration system is shown in Figure 5.18.

The distribution of ratio between the exergy destruction rate of a component and the total exergy destruction rate is shown in Figure 5.19.

Table 5.9 The values of physical exergy, chemical exergy, and total exergy for each point in the system

State	**Physical exergy, $\overline{ex}_i^{PH}$, kJ/kmol**	**Chemical exergy, $\overline{ex}_i^{CH}$, kJ/kmol**	**Total exergy, $\overline{ex}_i$, kJ/kmol**
1	0	8635	8635
2	419.3	8635	9054
3	419.3	8635	9054
4	1461	8635	10096
5	0	824350	824350
6	419.3	824350	824769
7	910.8	278962	279873
8	5610	218966	224576
9	2219	218966	221185
10	2256	206846	209102
11	1166	206846	208012
12	1238	175866	177104
13	419.3	61.04	480.4
14	419.3	61.04	480.4
15	1130	347.5	1478
16	436.3	347.5	783.8
17	419.3	61.04	480.4
18	419.3	8635	9054
19	420.5	8635	9056
20	421.1	8635	9056
21	1005	8635	9640
22	1324	8635	9959
23	2252	8635	10887
24	1158	0	1158
25	2250	0	2250
26	1158	0	1158
27	1158	0	1158
28	45289	2908	48196
29	5106	2908	8014
30	4044	2908	6951
31	882.3	2908	3790

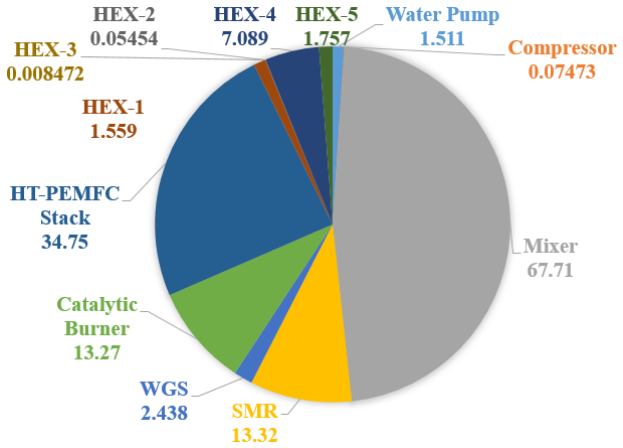

Figure 5.18 The ratio between the exergy destruction rate of a component and the exergy rate of the fuel supplied to cogeneration system (y_D)

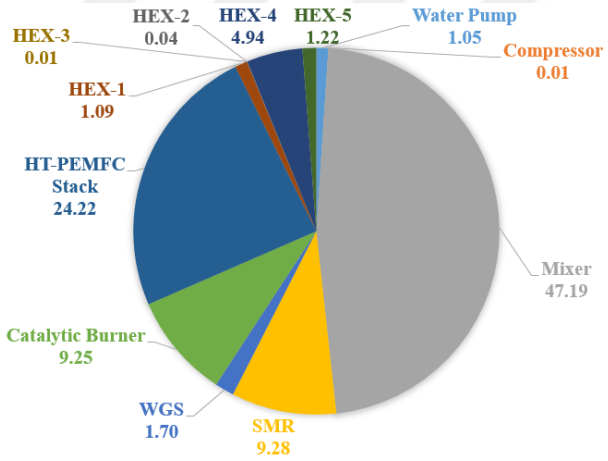

Figure 5.19 The ratio between the exergy destruction rate of a component and the total exergy destruction rate (y_D^*)

5.5.2.1 The effect of steam-to-carbon ratio on the exergy destruction of components and exergetic efficiency

Steam-to-carbon ratio is calculated using Eq. (5.2). As mentioned in Section 5.5.1.1, when the SCR increases from 1 to 2, the molar flow rate of CH_4 decreases and the molar flow rate of water increases very little. SCR affects the exergy destruction of each component as shown in Table 5.10.

When the SCR is changed from 1 to 2, the exergy destructions of water pump and HT-PEMFC stack are found to increase by 0.73% and 0.18%, respectively. Also, when the SCR is changed from 1 to 2, the exergy destructions of compressor, mixer, SMR, WGS, catalytic burner, and all heat exchangers are found to decrease by 48.64%, 32%, 19.96%, 8%, 67.83%, and 66%, respectively. Figure 5.20 shows the change of exergetic efficiency of the cogeneration system with SCR. The exergetic efficiency is calculated using Eq. (4.82). When the SCR changes from 1 to 2, the exergy of fuel supplied to the cogeneration system and the beneficial heat to produce hot water decrease by 48.65% and 92.29%, respectively. The net electrical power output of the cogeneration system increases by 2.62%. The numerator of the exergetic efficiency formulation (Eq. (4.82)) has decreased more than denominator. Therefore, when the SCR increases from 1 to 2, the exergetic efficiency of the cogeneration system decreases from 35.02% to 26.74%.

Table 5.10 The values of exergy destruction for each component according to SCR

SCR	$\dot{E}x_{D,pump}$, **kW**	$\dot{E}x_{D,comp}$, **kW**	$\dot{E}x_{D,mixer}$, **kW**	$\dot{E}x_{D,SMR}$, **kW**
1	76.01	0.6864	4669	785.2
1.222	76.11	0.5642	4220	766.3
1.444	76.21	0.4796	3854	742.6
1.667	76.32	0.418	3551	711.1
1.889	76.48	0.3715	3302	664
2	76.58	0.3525	3194	628.4
SCR	$\dot{E}x_{D,WGS}$, **kW**	$\dot{E}x_{D,burner}$, **kW**	$\dot{E}x_{D,fuelcell}$, **kW**	$\dot{E}x_{D,HEXtotal}$, **kW**
1	125	1946	1637	1433
1.222	115.1	1462	1638	1228
1.444	111.5	1128	1638	996.9
1.667	111.5	884.2	1639	770.1
1.889	113.6	700.7	1639	569.6
2	115	625.9	1640	488.3

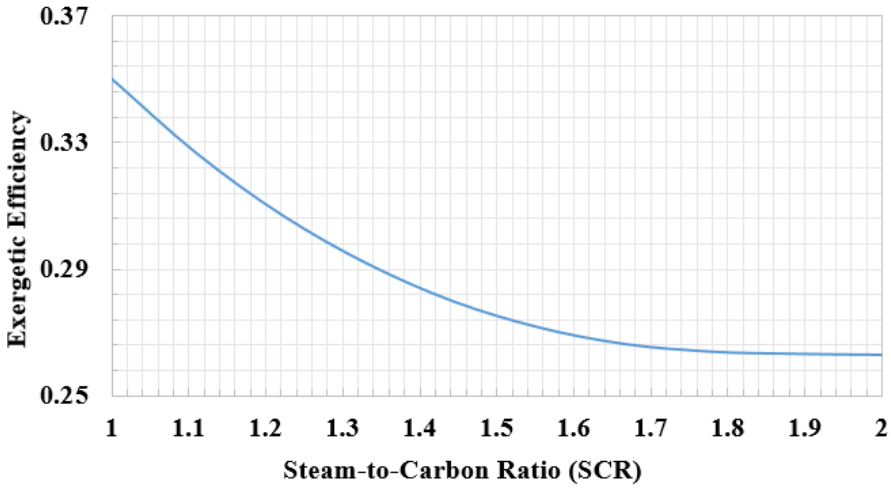

Figure 5.20 The change of exergetic efficiency with SCR

5.5.2.2 The effect of fuel cell operating temperature on the exergy destruction of components and exergetic efficiency

Table 5.11 shows the effects of the fuel cell operating temperature on the exergy destruction of each component. When the fuel cell operating temperature increases from 120°C to 200°C, the exergy destructions of water pump, compressor, mixer, and WGS do not change, however, the exergy destructions of SMR, catalytic burner, HT-PEMFC stack, and total heat exchangers change. The exergy destructions of catalytic burner, HT-PEMFC stack, and total heat exchangers decrease by 2.77%, 15.13%, and 16.04%, respectively. The exergy destruction of SMR increases 1.49%.

Figure 5.21 shows the effect of the fuel cell operating temperature on the exergetic efficiency of the cogeneration system. When the fuel cell operating temperature increases from 120°C to 200°C, the beneficial heat to produce hot water decrease by 6.09% and the net electrical power output of the cogeneration system increases by 37.21%. The numerator of the exergetic efficiency formulation (Eq. (4.82)) has increased at the fixed fuel exergy. Therefore, the exergetic efficiency increases from 22.26% to 30.02%.

Table 5.11 The values of exergy destruction for each component according to the fuel cell operating temperature

T_{cell} (°C)	$\dot{E}x_{D,pump}$, kW	$\dot{E}x_{D,comp}$, kW	$\dot{E}x_{D,mixer}$, kW	$\dot{E}x_{D,SMR}$, kW
120	76.58	0.3525	3194	623.7
137.8	76.58	0.3525	3194	625.8
146.7	76.58	0.3525	3194	626.8
164.4	76.58	0.3525	3194	628.9
182.2	76.58	0.3525	3194	631
191.1	76.58	0.3525	3194	632
200	76.58	0.3525	3194	633
T_{cell} (°C)	$\dot{E}x_{D,WGS}$, kW	$\dot{E}x_{D,burner}$, kW	$\dot{E}x_{D,fuelcell}$, kW	$\dot{E}x_{D,HEXtotal}$, kW
120	115	635.1	1797	537.8
137.8	115	630.9	1717	512.8
146.7	115	628.8	1684	502.5
164.4	115	624.9	1626	483.9
182.2	115	621.1	1573	467
191.1	115	619.3	1549	459
200	115	617.5	1525	451.1

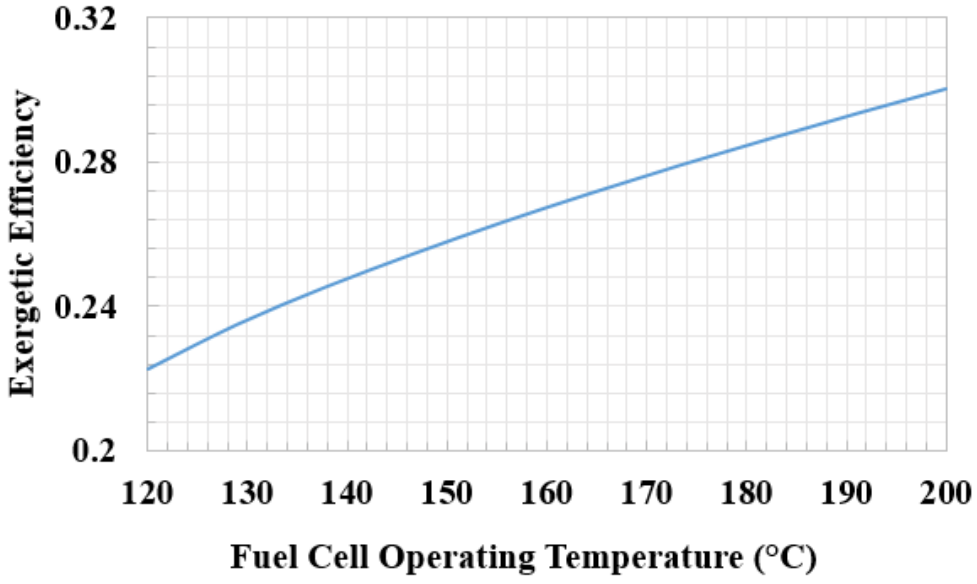

Figure 5.21 The change of exergetic efficiency due to fuel cell operating temperature

5.5.2.3 The effect of anode stoichiometric ratio on the exergy destruction of components and exergetic efficiency

The importance of the anode stoichiometric ratio on the performance of the cogeneration system is mentioned in the Section 5.5.1.3. Table 5.12 shows the change of the exergy destruction of each component in the system with changing anode stoichiometric ratio. When the anode stoichiometric ratio changes from 1.2 to 2, the increases of the exergy destruction of the water pump, compressor, mixer, SMR, WGS, catalytic burner, HT-PEMFC stack, and total heat exchangers are found as 19.17%, 68.79%, 68.78%, 70.75%, 66.60%, 72.39%, 82.6%, and 20.41%, respectively. Figure 5.22 shows the effect of the anode stoichiometric ratio on the exergetic efficiency of the cogeneration system. When the anode stoichiometric ratio increases from 1.2 to 2, the exergetic efficiency decreases from 26.74% to 16.74%.

Table 5.12 The values of exergy destruction for each component according to the anode stoichiometric ratio

λ_{H_2}	$\dot{E}x_{D,pump}$, kW	$\dot{E}x_{D,comp}$, kW	$\dot{E}x_{D,mixer}$, kW	$\dot{E}x_{D,SMR}$, kW
1.2	76.58	0.3525	3194	628.4
1.3	78.4	0.3825	3466	683.1
1.4	80.22	0.4127	3739	738.1
1.5	82.05	0.4429	4013	793.4
1.6	83.88	0.4731	4287	848.8
1.7	85.72	0.5035	4562	904.5
1.8	87.56	0.5339	4838	960.3
1.9	89.41	0.5644	5114	1016
2	91.26	0.595	5391	1073
λ_{H_2}	$\dot{E}x_{D,WGS}$, kW	$\dot{E}x_{D,burner}$, kW	$\dot{E}x_{D,fuelcell}$, kW	$\dot{E}x_{D,HEXtotal}$, kW
1.2	115	625.9	1640	488.3
1.3	124.6	681.2	1911	501.6
1.4	134.2	737	2182	514.7
1.5	143.7	793.1	2453	527.4
1.6	153.3	849.5	2724	539.8
1.7	162.9	906.3	2996	552
1.8	172.5	963.5	3267	563.8
1.9	182	1021	3538	575.4
2	191.6	1079	3809	586.6

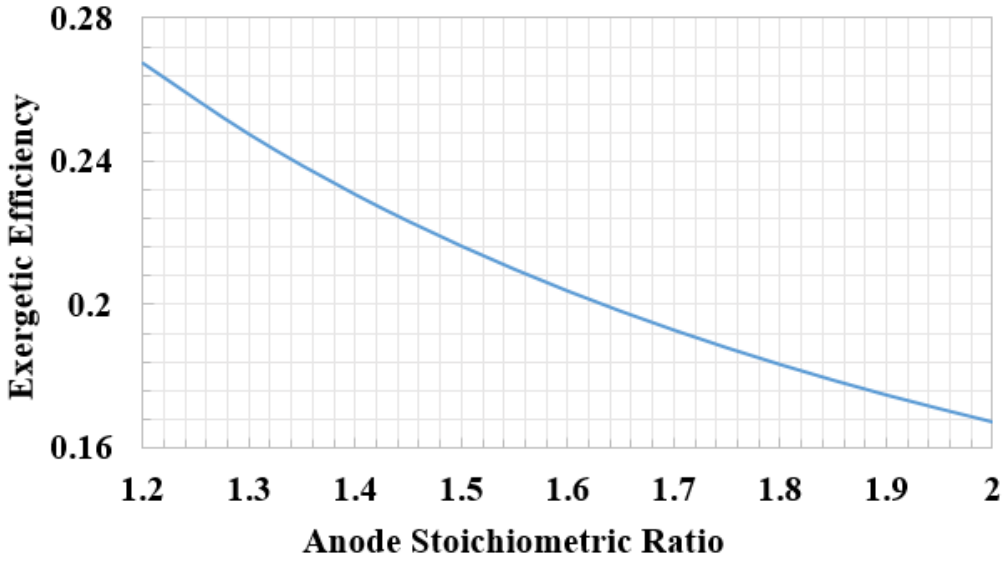

Figure 5.22 The change of exergetic efficiency due to anode stoichiometric ratio

CHAPTER SIX
CONCLUSIONS

In this thesis, firstly, a one-dimensional and semi-empirical model for a HT-PEMFC was developed. Diffusion mechanism of multicomponent gas flows through the GDL were represented by the Stefan-Maxwell equation for both anode and cathode sides; and the mole fractions of the reactant gases (H_2 and O_2) at the interface of GDL and catalyst layer were found. Then, Henry's Law and Fick's Law were used to find the concentrations of H_2 and O_2 on Pt catalyst surface using thin electrolyte film assumption. Thus, the cell voltage was calculated based on these concentrations. Three modeling parameters (the thin electrolyte film thicknesses for anode and cathode sides and the contact resistance) were calibrated using the experimental data. The HT-PEMFC is modeled for both PBI binder and PVDF binder. The effects of operating cell temperature (160°C, 180°C, and 200°C) and the effect of amount of CO were investigated in the HT-PEMFC model based on PBI binder. The effects of Pt loadings (0.6 mg/cm^2, 1 mg/cm^2 and 1.5 mg/cm^2), percentage of PA (70%, 75%, 80%, 85%, and 90%), and operation cell temperature (160°C, 180°C, and 200°C) were investigated in the HT-PEMFC model based on PVDF binder. Finally, the effect of the different binders (PBI and PVDF) on the performance of fuel cell were investigated.

The main findings derived from the model of HT-PEMFC based on PBI binder are as follows:

- When the operating temperature increases, the performance of fuel cell increases. The power density at 0.5 V was calculated as 0.25 W/cm^2, 0.28 W/cm^2 and 0.31 W/cm^2 at 160°C, 180°C and 200°C, respectively. The increase ratio of power density was 24% if the cell temperature was raised from 160°C to 200°C.
- When CO percentage in reformate gas increases, the performance of fuel cell decreases. When the CO percentage is changed from 1% CO to 5% CO, the cell voltage decreased by 1.07% for 160°C whereas the cell voltage decreased by

0.45% for 200°C. Thus, when the temperature increases, the effect of amount of CO on the performance of the fuel cell decreases.

The main findings derived from the model of HT-PEMFC based on PVDF binder are as follows:

- When the Pt loading increases from 0.6 mg/cm^2 to 1.5 mg/cm^2, the increase of power density at 0.5V is found to be 46%.
- When the percentage of PA changes from 70% to 85%, the performance of the fuel cell increases. However, the performance decreases when more than 85% of PA is used due to the decrease in the diffusion coefficient and the increase in the Henry's constant.
- When the operating cell temperature increases from 160°C to 200°C, the increase of power density at 0.5 V was found to be 17.55%.
- The performance of the fuel cell using PVDF binder exhibited better performance as compared to that using PBI binder.
- The thin film thickness affects the concentrations of H_2 and O_2 on the Pt surface. When the thin film thickness decreases, the performance of the fuel cell increases.

Secondly, a mathematical model of a cogeneration system, which includes a semi-empirical modeled HT-PEMFC stack, a heat exchanger, and a pump, is developed. This model is validated using the experimental results such as the temperature difference between the inlet and outlet coolant streams and the fuel utilization efficiency. The effect of anode stoichiometry ratio on the electrical and fuel utilization efficiencies were investigated. Moreover, the temperature of hot water used for the household needs was calculated for different current densities and number of cells in the stack. The main findings derived from this study are as follows.

- When the anode stoichiometry ratio increases, the electrical and fuel utilization efficiencies decrease. The decrease of fuel utilization efficiency at 0.42 A/cm2 is found to be 54% when the anode stoichiometry ratio increases from 1.2 to 2.5.
- When both the current density and number of cells increase, the hot water

temperature increases.

- HT-PEMFC stack-based cogeneration system is suitable for the fundamental needs in the house.

Thirdly, the energy and exergy analyses of the cogeneration system including the fuel processing system (SMR, WGS, and catalytic burner), HT-PEMFC power system and auxiliary components (water pump, compressor, air blower, and heat exchangers) were examined. The modeling equations were solved using EES software. The effects of steam-to-carbon ratio, operating cell temperature, and anode stoichiometric ratio on the performance of the cogeneration system (electrical efficiency and cogeneration efficiency) were investigated in the energy analysis. An exergy analysis of the HT-PEMFC based cogeneration system that produces hot water and electricity was conducted. The exergy destructions of each component in the system were calculated. The effects of steam-to-carbon ratio, fuel cell operating temperature, and anode stoichiometric ratio on the exergy efficiency of the cogeneration system were assessed.

The main conclusions derived from the energy analysis for the integrated cogeneration system are listed as follows:

- When the SCR ratio is increased from 1 to 2, the electrical efficiency increases from 13.21% to 26.4%, while the cogeneration efficiency decreases from 83.03% to 70.32%.
- When the fuel cell operating temperature increases from 120 ° C to 200 ° C, the system's electrical efficiency and cogeneration efficiency increase by 37.21% and decrease by 0.35%, respectively.
- When the anode stoichiometric ratio is increase from 1 to 2, the electrical efficiency and cogeneration efficiency decrease by 52.08% and 42.86%, respectively.

The main conclusions derived from the exergy analysis for the integrated cogeneration system are listed as follows:

- When the SCR is changed from 1 to 2, the exergy destructions of water pump and HT-PEMFC stack are found to increase by 0.73% and 0.18%, respectively. Also, when the SCR is changed from 1 to 2, the exergy destructions of compressor, mixer, SMR, WGS, catalytic burner, and all heat exchangers are found to decrease by 48.64%, 32%, 19.96%, 8%, 67.83%, and 66%, respectively.
- When the SCR increases from 1 to 2, the exergetic efficiency of the cogeneration system decreases from 43.2% to 30.3%.
- When the fuel cell operating temperature increases from 120°C to 200°C, the exergy destructions of water pump, compressor, mixer, and WGS do not change, however, the exergy destructions of SMR, catalytic burner, HT-PEMFC stack, and total heat exchangers change. The exergy destructions of catalytic burner, HT-PEMFC stack, and total heat exchangers decrease by 2.77%, 15.13%, and 16.04%, respectively. The exergy destruction of SMR increases by 1.49%.
- When the fuel cell operating temperature increases from 120°C to 200°C, the exergetic efficiency increases from 25.86% to 33.45%.
- When the anode stoichiometric ratio changes from 1.2 to 2, the increases of the exergy destruction of the water pump, compressor, mixer, SMR, WGS, catalytic burner, HT-PEMFC stack, and total heat exchangers are found as 19.17%, 68.79%, 68.78%, 70.75%, 66.60%, 72.39%, 82.6%, and 20.41%, respectively.
- When the anode stoichiometric ratio increases from 1.2 to 2, the exergetic efficiency decreases from 30.25% to 20.01%.

REFERENCES

Al-Baghdadi, M. A. S. (2015). Mechanical behaviour of membrane electrode assembly (MEA) during cold start of PEM fuel cell from sub-zero environment temperature. *International Journal of Energy and Environment, 6* (2), 107.

Arsalis, A., Kær, S. K., & Nielsen, M. P. (2015). Modeling and optimization of a heat-pump-assisted high temperature proton exchange membrane fuel cell micro-combined-heat-and-power system for residential applications. *Applied Energy*, 147, 569-581.

Arsalis, A., Nielsen, M. P., & Kær, S. K. (2011). Modeling and parametric study of a 1 kWe HT-PEMFC-based residential micro-CHP system. *International Journal of Hydrogen Energy, 36* (8), 5010-5020.

Arsalis, A., Nielsen, M. P., & Kær, S. K. (2012). Modeling and optimization of a 1 kWe HT-PEMFC-based micro-CHP residential system. *International Journal of Hydrogen Energy, 37* (3), 2470-2481.

Authayanun, S., Saebea, D., Patcharavorachot, Y., Assabumrungrat, S., & Arpornwichanop, A. (2017). Optimal design of different reforming processes of the actual composition of bio-oil for high-temperature PEMFC systems. *International Journal of Hydrogen Energy, 42* (4), 1977-1988.

Barbir F. (2005). *PEM fuel cells theory and practice.* New York: Elsevier Academic Press.

Besancon, B. M., Hasanov, V., Imbault-Lastapis, R., Benesch, R., Barrio, M., & Mølnvik, M. J. (2009). Hydrogen quality from decarbonized fossil fuels to fuel cells. *International Journal of Hydrogen Energy, 34* (5), 2350-2360.

Bhadra, S., Kim, N. H., & Lee, J. H. (2010). A new self-cross-linked, net-structured, proton conducting polymer membrane for high temperature proton exchange membrane fuel cells. *Journal of Membrane Science, 349* (1-2), 304-311.

Bose, S., Kuila, T., Nguyen, T. X. H., Kim, N. H., Lau, K. T., & Lee, J. H. (2011). Polymer membranes for high temperature proton exchange membrane fuel cell: recent advances and challenges. *Progress in Polymer Science, 36* (6), 813-843.

Bouchet, R., & Siebert, E. (1999). Proton conduction in acid doped polybenzimidazole. *Solid State Ionics*, *118* (3-4), 287-299.

Brodt, M., Wycisk, R., Dale, N., & Pintauro, P. (2016). Power Output and Durability of Electrospun Fuel Cell Fiber Cathodes with PVDF and Nafion/PVDF Binders. *Journal of the Electrochemical Society*, *163* (5), F401-F410.

Butler, J. (2009). *Portable fuel cell survey.* Fuel Cell Today, UK, April.

Caglayan, D. G., Sezgin, B., Devrim, Y., & Eroglu, I. (2016). Three-dimensional modeling of a high temperature polymer electrolyte membrane fuel cell at different operation temperatures. *International Journal of Hydrogen Energy*, *41*(23), 10060-10070.

Candusso, D., Harel, F., De Bernardinis, A., Francois, X., Péra, M. C., Hissel, D., & Kauffmann, J. M. (2006). Characterisation and modelling of a 5 kW PEMFC for transportation applications. *International Journal of Hydrogen Energy*, *31* (8), 1019-1030.

Chang, H., Wan, Z., Zheng, Y., Chen, X., Shu, S., Tu, Z., & Chan, S. H. (2017). Energy analysis of a hybrid PEMFC–solar energy residential micro-CCHP system combined with an organic Rankine cycle and vapor compression cycle. *Energy Conversion and Management,* 142, 374-384.

Cheddie, D., & Munroe, N. (2006). Parametric model of an intermediate temperature PEMFC. *Journal of Power Sources, 156* (2), 414-423.

Cheddie, D. F., & Munroe, N. D. (2007). A two-phase model of an intermediate temperature PEM fuel cell. *International Journal of Hydrogen Energy, 32* (7), 832-841.

Chen, W. H., Lin, M. R., Jiang, T. L., & Chen, M. H. (2008). Modeling and simulation of hydrogen generation from high-temperature and low-temperature water gas shift reactions. *International Journal of Hydrogen Energy, 33* (22), 6644-6656.

Chippar, P., & Ju, H. (2013). Numerical modeling and investigation of gas crossover effects in high temperature proton exchange membrane (PEM) fuel cells. *International Journal of Hydrogen Energy, 38* (18), 7704-7714.

Colpan, C. O., Nalbant, Y., & Ercelik, M. (2018). *4.28 Fundamentals of Fuel Cell Technologies.* Inpress.

Das, S., Dutta, K., & Kundu, P. P. (2015). Nickel nanocatalysts supported on sulfonated polyaniline: potential toward methanol oxidation and as anode materials for DMFCs. *Journal of Materials Chemistry A, 3* (21), 11349-11357.

Devrim, Y., Albostan, A., & Devrim, H. (2018). Experimental investigation of CO tolerance in high temperature PEM fuel cells. *International Journal of Hydrogen Energy*. Inpress

Devrim, Y., Devrim, H., & Eroglu, I. (2016). Polybenzimidazole/SiO2 hybrid membranes for high temperature proton exchange membrane fuel cells. *International Journal of Hydrogen Energy, 41* (23), 10044-10052.

Dhar, H. P., Kush, A. K., Patel, D. N., & Christner, L. G. (1986). Modeling for CO poisoning of a fuel cell anode. *In Electrochemical and Thermal Modeling of Battery, Fuel Cell, and Photoenergy Conversion Systems*, 284-297.

Ercelik M. (2017). *Manufacturing and testing of direct methanol fuel cells based on alternative materials.* Ms.C. thesis. Dokuz Eylül University, Turkey.

Ergun, D., Devrim, Y., Bac, N., & Eroglu, I. (2012). Phosphoric acid doped polybenzimidazole membrane for high temperature PEM fuel cell. *Journal of Applied Polymer Science, 124* (S1).

Galbiati, S., Coulon, P. E., Rizza, G., Clochard, M. C., Castellino, M., Sangermano, M., ... & Morin, A. (2015). Poly (vinylimidazole) radiografted PVDF nanospheres as alternative binder for high temperature PEMFC electrodes. *Journal of Power Sources*, 296, 117-121.

Herdem, M. S., Farhad, S., & Hamdullahpur, F. (2015). Modeling and parametric study of a methanol reformate gas-fueled HT-PEMFC system for portable power generation applications. *Energy Conversion and Management*, 101, 19-29.

Holst-Olesen, K., Nesselberger, M., Perchthaler, M., Hacker, V., & Arenz, M. (2014). Activity inhibition and its mitigation in high temperature proton exchange membrane fuel cells: The role of phosphoric acid, ammonium trifluoromethanesulfonate, and polyvinylidene difluoride. *Journal of Power Sources*, 272, 1072-1077.

Hou, K., & Hughes, R. (2001). The kinetics of methane steam reforming over a Ni/α-Al2O catalyst. *Chemical Engineering Journal, 82* (1-3), 311-328.

Jannelli, E., Minutillo, M., & Perna, A. (2013). Analyzing microcogeneration systems based on LT-PEMFC and HT-PEMFC by energy balances. *Applied Energy*, 108, 82-91.

Kazim, A. (2004). Exergy analysis of a PEM fuel cell at variable operating conditions. *Energy conversion and management, 45* (11-12), 1949-1961.

Kim, S., Myles, T. D., Kunz, H. R., Kwak, D., Wang, Y., & Maric, R. (2015). The effect of binder content on the performance of a high temperature polymer electrolyte membrane fuel cell produced with reactive spray deposition technology. *Electrochimica Acta*, 177, 190-200.

Krastev, V. K., Falcucci, G., Jannelli, E., Minutillo, M., & Cozzolino, R. (2014). 3D CFD modeling and experimental characterization of HT PEM fuel cells at different anode gas compositions. *International Journal of Hydrogen Energy, 39* (36), 21663-21672.

Krumpelt, M., Krause, T. R., Carter, J. D., Kopasz, J. P., & Ahmed, S. (2002). Fuel processing for fuel cell systems in transportation and portable power applications. *Catalysis Today, 77* (1-2), 3-16.

Liang, H., Su, H., Pollet, B. G., & Pasupathi, S. (2015). Development of membrane electrode assembly for high temperature proton exchange membrane fuel cell by catalyst coating membrane method. *Journal of Power Sources*, 288, 121-127.

Lin, H. L., Wu, T. J., Lin, Y. T., & Wu, H. C. (2015). Effect of polyvinylidene difluoride in the catalyst layer on high-temperature PEMFCs. *International Journal of Hydrogen Energy, 40* (30), 9400-9409.

Mamlouk, M., Sousa, T., & Scott, K. (2011). A high temperature polymer electrolyte membrane fuel cell model for reformate gas. *International Journal of Electrochemistry.*

Mench MM. (2008). *Fuel Cell Engines.* Doi: 10.1002/9780470209769.

Moran, M. J., Shapiro, H. N., Boettner, D. D., & Bailey, M. B. (2010). *Fundamentals of engineering thermodynamics.* John Wiley & Sons.

Najafi, B., Mamaghani, A. H., Rinaldi, F., & Casalegno, A. (2015). Long-term performance analysis of an HT-PEM fuel cell based micro-CHP system: operational strategies. *Applied Energy*, 147, 582-592.

Nalbant, Y., Colpan, C. O., & Devrim, Y. (2017). Development of a one-dimensional and semi-empirical model for a high temperature proton exchange membrane fuel cell. *International Journal of Hydrogen Energy.*

Okur, O., Karadağ, Ç. İ., San, F. G. B., Okumuş, E., & Behmenyar, G. (2013). Optimization of parameters for hot-pressing manufacture of membrane electrode assembly for PEM (polymer electrolyte membrane fuel cells) fuel cell. *Energy*, 57, 574-580.

Oliveira, E. L., Grande, C. A., & Rodrigues, A. E. (2009). Steam methane reforming in a Ni/Al2O3 catalyst: kinetics and diffusional limitations in extrudates. *The Canadian Journal of Chemical Engineering, 87* (6), 945-956.

Orogbemi, O. M., Ingham, D. B., Ismail, M. S., Hughes, K. J., Ma, L., & Pourkashanian, M. (2017). On the gas permeability of the microporous layer used in polymer electrolyte fuel cells. *Journal of the Energy Institute.*

Özgirgin, E., Devrim, Y., & Albostan, A. (2015). Modeling and simulation of a hybrid photovoltaic (PV) module-electrolyzer-PEM fuel cell system for micro-cogeneration applications. *International Journal of Hydrogen Energy*, *40* (44), 15336-15342.

Perera, F. P. (2017). Multiple threats to child health from fossil fuel combustion: impacts of air pollution and climate change. *Environmental Health Perspectives*, *125* (2), 141.

Ren, X., Zelenay, P., Thomas, S., Davey, J., & Gottesfeld, S. (2000). Recent advances in direct methanol fuel cells at Los Alamos National Laboratory. *Journal of Power Sources, 86* (1-2), 111-116.

Rosli, R. E., Sulong, A. B., Daud, W. R. W., Zulkifley, M. A., Husaini, T., Rosli, M. I., ... & Haque, M. A. (2017). A review of high-temperature proton exchange membrane fuel cell (HT-PEMFC) system. *International Journal of Hydrogen Energy, 42* (14), 9293-9314.

Scott, K., Pilditch, S., & Mamlouk, M. (2007). Modelling and experimental validation of a high temperature polymer electrolyte fuel cell. *Journal of Applied Electrochemistry, 37* (11), 1245-1259.

Slattery, J. C., & Bird, R. B. (1958). Calculation of the diffusion coefficient of dilute gases and of the self-diffusion coefficient of dense gases. *AIChE Journal, 4* (2), 137-142.

Sezgin, B., Caglayan, D. G., Devrim, Y., Steenberg, T., & Eroglu, I. (2016). Modeling and sensitivity analysis of high temperature PEM fuel cells by using Comsol Multiphysics. *International Journal of Hydrogen Energy, 41* (23), 10001-10009.

Shamardina, O., Chertovich, A., Kulikovsky, A. A., & Khokhlov, A. R. (2010). A simple model of a high temperature PEM fuel cell. *International Journal of Hydrogen Energy, 35* (18), 9954-9962.

Sohn, Y. J., Park, G. G., Yang, T. H., Yoon, Y. G., Lee, W. Y., Yim, S. D., & Kim, C. S. (2005). Operating characteristics of an air-cooling PEMFC for portable applications. *Journal of Power Sources, 145* (2), 604-609.

Sousa, T., Mamlouk, M., & Scott, K. (2010). An isothermal model of a laboratory intermediate temperature fuel cell using PBI doped phosphoric acid membranes. *Chemical Engineering Science, 65* (8), 2513-2530.

Su, H., Pasupathi, S., Bladergroen, B., Linkov, V., & Pollet, B. G. (2013a). Optimization of gas diffusion electrode for polybenzimidazole-based high temperature proton exchange membrane fuel cell: evaluation of polymer binders in catalyst layer. *International Journal of Hydrogen Energy, 38* (26), 11370-11378.

Su, H., Pasupathi, S., Bladergroen, B., Linkov, V., & Pollet, B. G. (2013b). Performance investigation of membrane electrode assemblies for high temperature proton exchange membrane fuel cell. *Journal of Power and Energy Engineering, 1* (05), 95.

Sun, W., Peppley, B. A., & Karan, K. (2005). An improved two-dimensional agglomerate cathode model to study the influence of catalyst layer structural parameters. *Electrochimica acta, 50* (16-17), 3359-3374.

Supra, J., Janßen, H., Lehnert, W., & Stolten, D. (2013). Temperature distribution in a liquid-cooled HT-PEFC stack. *International Journal of Hydrogen Energy, 38* (4), 1943-1951.

Ubong, E. U., Shi, Z., & Wang, X. (2009). Three-dimensional modeling and experimental study of a high temperature PBI-based PEM fuel cell. *Journal of the Electrochemical Society, 156* (10), B1276-B1282.

Wang, Y., Chen, K. S., Mishler, J., Cho, S. C., & Adroher, X. C. (2011). A review of polymer electrolyte membrane fuel cells: technology, applications, and needs on fundamental research. *Applied energy, 88* (4), 981-1007.

Wee, J. H. (2007). Applications of proton exchange membrane fuel cell systems. *Renewable and Sustainable Energy Reviews, 11* (8), 1720-1738.

Wilson, M. S., & Gottesfeld, S. (1992). Thin-film catalyst layers for polymer electrolyte fuel cell electrodes. *Journal of Applied Electrochemistry, 22* (1), 1-7.

Wu, H. W. (2016). A review of recent development: Transport and performance modeling of PEM fuel cells. *Applied Energy*, 165, 81-106.

Xu, J., & Froment, G. F. (1989). Methane steam reforming, methanation and water-gas shift: I. Intrinsic kinetics. *AIChE journal*, *35* (1), 88-96.

Zamel, N. (2016). The catalyst layer and its dimensionality–A look into its ingredients and how to characterize their effects. *Journal of Power Sources*, 309, 141-159.

Zhang, C., Yu, T., Yi, J., Liu, Z., Raj, K. A. R., Xia, L., & Chan, S. H. (2016). Investigation of heating and cooling in a stand-alone high temperature PEM fuel cell system. *Energy Conversion and Management*, 129, 36-42.

APPENDIX

Nomenclature

Abbreviations

ACL	Anode catalyst layer
AGDL	Anode gas diffusion layer
C	Carbon
CCL	Cathode catalyst layer
CGDL	Cathode gas diffusion layer
EG	Ethylene glycol
FC	Fuel cell
FUE	Fuel utilization efficiency
GDL	Gas diffusion layer
HEX	Heat exchanger
HTS	High-temperature shift
LTS	Low-temperature shift
M	Membrane
MEA	Membrane electrode assembly
PBI	Polybenzimidazole
PVDF	Polyvinylidene fluoride
SMR	Steam-methane reformer
SCR	Steam-to-carbon ratio
WGS	Water-Gas Shift

Variables

a	Activity
a_c	Catalyst surface area, $\mathrm{cm}^2_{\mathrm{real}}/\mathrm{mg}_{\mathrm{Pt}}$

A_{cell}	Active area of the cell, cm^2
A_i	Pre-exponential factor of rate coefficient of reaction, i
ASR	Area specific resistance, Ω
$\overline{c_p}$	Specific heat constant, kJ/kmol·K
$C_{dissolved}$	Equilibrium concentration, mol/cm^3
C_{Pt}	Concentration on the Pt surface, mol/cm^3
C_{Pt}^{ref}	Reference concentration on the Pt surface, mol/cm^3
D_{ij}^{eff}	Binary diffusion coefficient, cm^2/s
D^{PA}	Diffusion through phosphoric acid ionomer, cm^2/s
DEN	The adsorption of reacting species onto the active catalyst sites
ex_i	The exergy of a flowing stream i, kJ/kmol
E_c	Activation energy, J/mol
E_i	Activation energy of reaction, i
E_{cell}	Cell voltage, V
E_{rev}	Reversible cell potential, V
E_{stack}	Stack voltage, V
$\dot{Ex}$	Exegy, kW
$\dot{Ex}_D$	Exergy destruction, kW
F	Faraday constant, 96,485 $C \cdot mol^{-1}$
$\bar{h}_i$	Enthalpy of i
H^{PA}	Henry's constant of species in concentrated phosphoric acid, $cm^3 \cdot mPa/mol$
Δh_i	Specific enthalpy change of reaction i, kJ/kmol
i	Current density, A/cm^2
i_0	Exchange current density, A/cm^2
i_0^{ref}	Reference exchange current density, A/cm^2
Kj	Adsorption constant for species, j
Kp_i	Equilibrium constant of reaction, i
L_c	Catalyst loading, mg_{Pt}/cm^2_{active}
L_{PA}	The mass of phosphoric acid per area, mg/cm^2
$\overline{LHV}$	Lower heating value, kJ/kmol

M_i	The molecular weight of the gas, g/mol
m^{PA}	The weight percentage of phosphoric acid
$\dot{n}_i^{"}$	Molar flux of species i, mol/cm^2-s
N_{cell}	Number of cells
n	The scaling factor
P	Pressure, mPa
P_{cr}	Critical pressure of gas, mPa
$\dot{Q}$	Heat transfer rate, kW
$\dot{Q}_{hotwater}$	The beneficial heat to produce hot water, kW
R	Gas constant, J/mol·K
$R_{contact}$	Contact resistance, Ω·cm^2
r_{agg}	Agglomerate radius, cm
r_i	Rate of reaction, i (mol/kg·s)
S	The specific surface area per unit area (a·L)
T_{cell}	Cell temperature, K
T_{cr}	Critical temperature of gas, K
T_{ref}	Reference cell temperature, K
t	Thickness, cm
$\forall_{ionomer}$	Volume of ionomer, cm^3
$\dot{W}$	Power, kW
X_i^0	Input molar fraction of species i
X_i	The molar fraction of species i
y_D	The ratio between the exergy destruction rate of a component and the exergy rate of the fuel
y_D^*	The ratio between the exergy destruction rate of component and total exergy destruction rate

Greeks Letters

α	Transfer coefficient
γ	Reaction order

δ	Average ionomer film thickness covering a catalyst particle, cm
ε	The porosity
ε_{ex}	Exergy efficiency
η	Over potential, V
θ_{CO}	CO coverage
λ	Stoichiometric ratio
ρ	Density, kg/m^3
σ	Conductivity, S/cm
τ	The tortuosity

Subscript/Superscript

a	Anode
act	Activation
agg	Agglomerate
CH	Chemical
CH_4	Methane
CO	Carbon monoxide
CO_2	Carbon dioxide
c	Cathode
comp	Compressor
cv	Control volume
e	Electron
gen	Generated
H_2	Hydrogen
H_2O	Water
i	Reaction number
j	Species
in	Input
O_2	Oxygen
out	Output